POLITECNICO DI TORINO
Repository ISTITUZIONALE

Generalized Analytical Models of Filtering Penalties and Equalization in Coherent Optical Links

Original
Generalized Analytical Models of Filtering Penalties and Equalization in Coherent Optical Links / Miotto, E., Rosso, A., Straullu, S., Virgillito, E., Corsini, R., Bovio, A., Curri, V.. - In: IEEE OPEN JOURNAL OF THE COMMUNICATIONS SOCIETY. - ISSN 2644-125X. - ELETTRONICO. - 7:(2026), pp. 9405-9430. [10.1109/ojcoms.2026.3719514]

Availability:
This version is available at: 11583/3014349 since: 2026-08-11T14:25:44Z

Publisher:
IEEE

Published
DOI:10.1109/ojcoms.2026.3719514

Terms of use:

This article is made available under terms and conditions as specified in the corresponding bibliographic description in the repository

Publisher copyright

(Article begins on next page)

26 November 2026

IEEE Open Journal of the Communications Society

Received 12 May 2026; revised 21 July 2026; accepted 30 July 2026. Date of publication 3 August 2026; date of current version 10 August 2026.

Digital Object Identifier 10.1109/OJCOMS.2026.3719514

Generalized Analytical Models of Filtering Penalties and Equalization in Coherent Optical Links

ENRICO MIOTTO[1] (Graduate Student Member, IEEE), ANDREA ROSSO[1] (Graduate Student Member, IEEE), STEFANO STRAULLU[2] (Senior Member, IEEE), EMANUELE VIRGILLITO[1] (Senior Member, IEEE), RAFFAELE CORSINI[3], ANDREA BOVIO[3], AND VITTORIO CURRI[1] (Fellow, IEEE)

[1]Department of Electronics and Telecommunications, Politecnico di Torino, Turin 10129, Italy
[2]LINKS Foundation, Turin 10138, Italy
[3]SM-Optics, Cologno Monzese 20093, Italy

CORRESPONDING AUTHOR: E. MIOTTO (enrico.miotto@polito.it)

This work was supported by the European Union (EU) Horizon Project Smart European Networks for Sensing the Environment and Internet quality (SENSEI) under Grant 101189545.

ABSTRACT This paper presents a unified analytical framework for filtering-penalty assessment and receiver equalization in coherent optical links dominated by linear impairments. The formulation targets scalar amplitude filtering, under the assumption of negligible phase and polarization effects, and jointly accounts for cascaded optical filters, amplified spontaneous emission (ASE) noise, receiver-side transceiver impairments, anti-aliasing filtering, and digital equalization. Closed-form post-equalization signal-to-noise ratio (SNR) expressions are derived for the zero-forcing equalizer (ZFE), minimum mean-square error equalizer (MMSEE), and fractionally spaced equalizer (FSE), while semi-analytical matrix formulations are provided for the whitened finite-length equalizer (WFLE) and finite-length equalizer (FLE). The models include the colored noise induced by distributed ASE injection and optical filtering, and are generalized to arbitrary normalized transceiver-noise power spectral densities (PSDs). The resulting post-equalization SNR and Q-factor metrics are suitable for optical network digital twin (ONDT) applications and for measurement-based characterization of commercial transceivers. Time-domain simulations and experiments with two commercial transceivers confirm the accuracy of the proposed approach and support its applicability to filtering-aware performance estimation in coherent optical links.

INDEX TERMS Filtering penalty, mathematical modeling, metro-access network convergence, optical network digital twin, transceiver penalty.

I. INTRODUCTION

AS THE demand for high-capacity, low-latency communication continues to increase, metro and access optical networks have become a cornerstone of modern communication infrastructure [1]. In these systems, quality of transmission (QoT) is predominantly affected by linear impairments, while nonlinear propagation effects are typically less dominant because of the relatively short transmission distances and moderate optical power levels [2]. Among these impairments, filtering penalties introduced by cascaded wavelength-selective switches (WSSs) in reconfigurable optical add-drop multiplexers (ROADMs) play a critical role in determining end-to-end performance [3].

In parallel, significant progress has been made toward the development of optical network digital twins (ONDTs) [4], [5], supported by accurate fiber and amplifier descriptions and by transparent-lightpath approximations based on the Gaussian Model [6]. However, ONDT transmission models still require a disaggregated, accurate, and computationally tractable representation of filtering penalties. This need is particularly relevant in metro-access and converged optical networks, where cascaded filtering, receiver digital signal processing (DSP) and equalization, transceiver noise, and network configuration jointly affect QoT and cannot be reliably captured by static margins alone.

A preliminary non-peer-reviewed version of part of the analytical framework was made available in [7]. The present manuscript provides the archival journal treatment, consolidating and extending that modeling effort with a generalized formulation, simulation analysis, and commercial-transceiver validation. The proposed treatment explicitly includes transceiver impairments, rather than

© 2026 The Authors. This work is licensed under a Creative Commons Attribution 4.0 License.
For more information, see https://creativecommons.org/licenses/by/4.0/

limiting the analysis to optical filtering and amplified spontaneous emission (ASE) noise. It also adopts generic coherent-link performance metrics, such as post-equalization signal-to-noise ratio (SNR), which are suitable for ONDT applications and are not restricted to metrics tailored to specific scenarios. The resulting approach is formulated to be applicable to commercial transceivers, including cases in which their behavior must be inferred from measurement-based characterization.

The analysis starts from an optical-channel representation that includes cascaded optical filters, additive noise contributions from optical amplifiers and the transceiver, and receiver-side DSP. To jointly account for filtering penalties and transceiver impairments, we adopt a transceiver description based on [8] and [9], following the measurement-oriented approach successfully adopted in [10]. Within this description, several equalization strategies are treated within a unified framework, namely the zero-forcing equalizer (ZFE), minimum mean-square error equalizer (MMSEE), fractionally spaced equalizer (FSE), whitened finite-length equalizer (WFLE), and finite-length equalizer (FLE). For these cases, closed-form and semi-analytical expressions are derived to quantify the post-equalization SNR and the associated filtering penalties. A key generalization is that the equalization models account for an arbitrary normalized transceiver-noise power spectral density (PSD), rather than assuming a fixed or white transceiver-noise spectrum. Frequency- and time-domain representations are used to capture signal distortion, noise coloring, noise enhancement, and finite-equalizer effects.

The analytical results are assessed through time-domain simulations and experimental validation. The time-domain simulations use the framework and software of [11] to test the derived expressions under realistic and complex filtering conditions, providing insight into the behavior and limitations of the different equalizers. The experimental analysis compares theoretical predictions with measurements obtained using accurately modeled optical filters, as in [10]. It includes different commercial transceivers, received optical powers, modulation formats, and transceiver-noise conditions. The results show close agreement among theory, time-domain simulations, and experiments, supporting the applicability of the proposed approach to metro-access scenarios and to ONDT transmission-model enhancement.

Overall, the proposed approach provides a unified and tractable basis for receiver-performance assessment in the presence of filtering impairments, transceiver impairments, and receiver equalization. By harmonizing the treatment of ZFE, MMSEE, FSE, WFLE, and FLE, and by allowing arbitrary colored transceiver-noise PSDs within generic coherent-link QoT metrics, it enables filtering-aware performance estimation for commercial transceivers and supports integration into ONDTs for disaggregated and converged optical networks.

Notably, the most realistic equalizer models, i.e., WFLE and FLE, provide the closest match to the reference data.

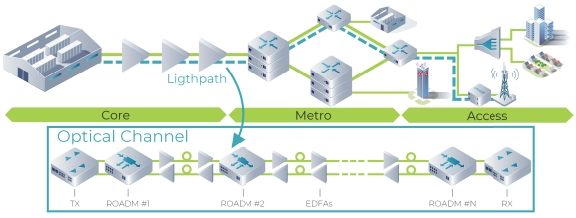

FIGURE 1. Optical channel scenario.

Their accuracy is confirmed by root-mean-square error (RMSE) values of 0.21 dB and 0.17 dB with respect to experimental measurements, and by an RMSE as low as 0.09 dB with respect to numerical simulations with 64 taps.

A. THE OPTICAL CHANNEL

In this work, we focus on a digital channel implemented by a transparent lightpath, the optical channel, investigating the combined effects of filtering, noise, transceiver impairments, and equalization. Many fundamental and well-established concepts from equalization theory and digital communications must be carefully adapted to the specific case of optical communications. A schematic of a transparent lightpath established through diverse optical network segments is depicted in Figure 1.

Our approach encompasses the evaluation of multiple types of impairments intrinsically related to the characteristics of the optical channel. Fiber propagation is a complex phenomenon due to nonlinear effects and stochastic polarization-related impairments; however, when using state-of-the-art dual-polarization coherent optical technologies, a transparent lightpath can be well approximated as a dual-polarization additive white Gaussian noise (DP-AWGN) channel [6], [12], [13].

In addition to physical effects, the considered framework is also specific in terms of the communication techniques adopted. In general, the analysis and modeling of a transparent lightpath must account for both the transmission technique and the physics of optical propagation. Optical communications based on transparent lightpaths leverage dual-polarization (DP) coherent transceiver technology, which enables compensation of linear propagation effects, such as chromatic dispersion and polarization rotations, through the DSP implemented in DP coherent transceivers (TRXs) [14], [15].

After DSP-based equalization compensates for linear propagation impairments, the optical channel can be described through an equivalent noise-accumulation model at the receiver. Accordingly, within the adopted DP-AWGN framework, the channel is modeled by jointly accounting for receiver noise, equalization effects, and accumulated propagation-related noise contributions.

Since coherent receivers effectively compensate for most linear propagation impairments, the main residual quality-of-transmission (QoT) penalties to account for are Kerr-effect-induced nonlinear crosstalk, also known as nonlinear interference (NLI) [16], [17], and amplified spontaneous

TABLE 1. Comparison of symbol rates and BER-formula coefficients k_1 and k_2 for the considered modulation formats and transceivers.

Modulation format	k_1, k_2	Vendor A	Vendor B
DP-QPSK 200G	$\frac{1}{2}$, $\frac{1}{2}$	63.1 GBd	69.4 GBd
DP-16QAM 200G	$\frac{3}{8}$, $\frac{1}{10}$	31.6 GBd	34.7 GBd
DP-16QAM 400G	$\frac{3}{8}$, $\frac{1}{10}$	63.1 GBd	69.4 GBd

emission (ASE) noise caused by optical amplification. In addition, optical switching at the ROADM level introduces filtering penalties, which translate into SNR degradation under the considered AWGN channel approximation. This work focuses on deriving the SNR penalties induced by filtering effects through accurate modeling of receiver noise and the equalization method.

Under the DP-AWGN approximation, the QoT of a transparent lightpath can be represented by its SNR. A comprehensive definition of the QoT considered in this work is provided in Section I-B, which follows the current one. In the considered model, the main noise contributions are ASE noise, transceiver noise, and NLI. ASE noise generated by optical amplification between ROADMs is distributed along the lightpath, whereas transceiver noise is modeled as concentrated at the receiver side. NLI is also treated under the DP-AWGN approximation as an equivalent noise source at the receiver, which represents a conservative assumption. As discussed later, the closer a noise source is to the receiver, the larger the filtering penalty associated with that contribution. We do not consider other impairments that can interact with filtering penalty, like polarization-dependent loss (PDL) and polarization-mode dispersion (PMD), because such analysis is out of the scope of this work. For further reference, it is worth mentioning that recent literature has begun addressing joint modeling of filtering penalties and polarization impairments, with some preliminary and promising insights [18].

System performance is evaluated in terms of the Q^2_{dB} factor [19], although the analytical models developed in the following provide results in terms of SNR. This choice reflects common practice in optical system evaluation, where Q^2_{dB} serves as a convenient performance indicator. The two metrics are directly related: SNR can be mapped to the bit-error rate (BER) through expressions that depend on the selected modulation format, and the corresponding Q^2_{dB} factor can then be derived from the BER as follows:

$$Q = \sqrt{2} \cdot \mathrm{erfcinv}(2 \cdot \mathrm{BER}) \tag{1}$$

$$Q^2_{dB} = 10 \log_{10}(Q^2) \tag{2}$$

Consequently, reporting results in terms of Q^2_{dB} does not imply a loss of generality, but rather provides an equivalent and easily interpretable representation of system performance.

B. TRANSCEIVER MODEL AND SNR DEFINITION

This section introduces a measurement-based methodology for modeling TRX performance that accounts for transceiver impairments when evaluating the filtering penalty. The focus is on accurately modeling the SNR and its impact on the BER, particularly in scenarios dominated by linear impairments, such as metro networks. In this work, the experimental validation was performed using two commercial transceivers, referred to as Vendor A and Vendor B. The considered formats include dual-polarization quadrature phase-shift keying (DP-QPSK) and dual-polarization 16-ary quadrature amplitude modulation (DP-16QAM). For each transceiver, the three modulation-format and bit-rate combinations, the corresponding symbol rates, and BER factors are reported in Table 1.

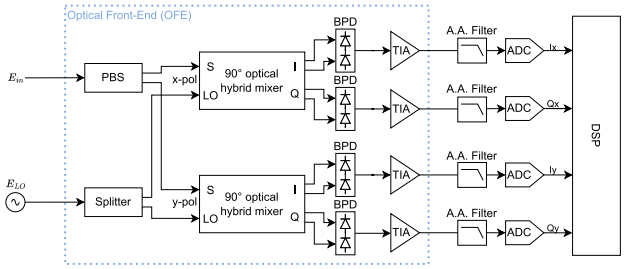

FIGURE 2. Realistic receiver block diagram. ADC: analog-to-digital converter; BPD: balanced photodetector; I: in-phase component; LO: local oscillator; PBS: polarization beam splitter; Q: quadrature component; TIA: transimpedance amplifier.

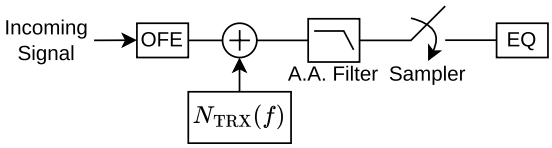

FIGURE 3. Receiver block diagram abstraction. AA: anti-aliasing filter; EQ: equalizer; OFE: optical front-end block.

Figure 2 shows a coherent optical transceiver front-end in which the received signal, after random polarization rotations, is split into two orthogonal polarization branches by a polarization beam splitter. Each polarization is mixed with a local oscillator in a 90° optical hybrid, producing in-phase and quadrature components that are detected by balanced photodetectors. The resulting electrical currents are amplified by transimpedance amplifiers, passed through anti-aliasing (AA) filters, and digitized by parallel analog-to-digital converters (ADCs) for both x- and y-polarization states. The digital samples are then processed by the DSP stage to recover the transmitted information. To facilitate the analysis of filtering penalties, we adopt a simplified transceiver representation that preserves the impact of receiver impairments and the equalization strategy, while remaining tractable for system-level discussion.

The block diagram of the transceiver model is provided in Figure 3. The transceiver is represented by grouping the main physical and digital stages into equivalent functional blocks. The incoming signal is first processed by an equivalent ideal optical front-end (OFE), performing optical-to-electrical (O/E) conversion. The impairments of the realistic OFE of Figure 2 are summarized through an aggregated receiver noise contribution. In addition, it is assumed that transmitter impairments are generally much smaller than receiver impairments, according to [7], [10], and [20]. Therefore, all

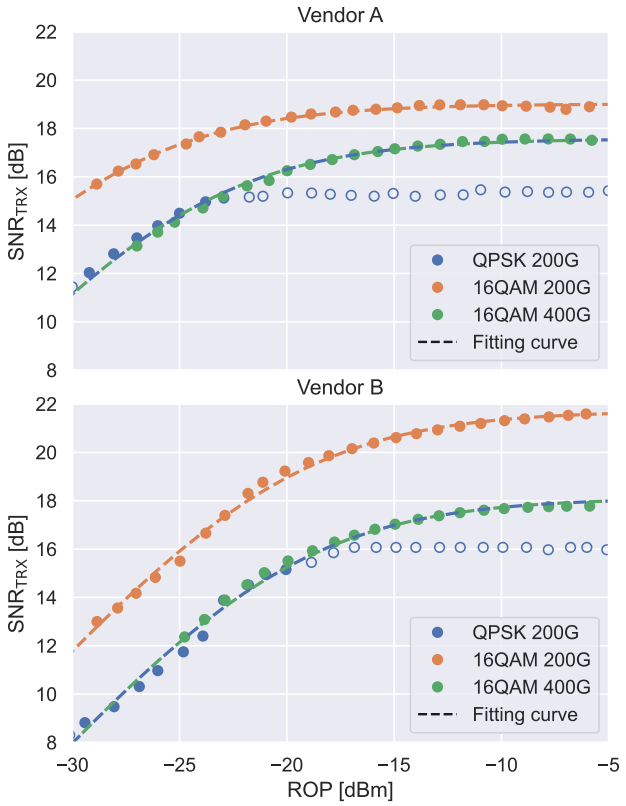

FIGURE 4. Back-to-back characterization of the transceivers.

the transceiver noise is assumed to be concentrated on the receiver side.

The resulting electrical signal then passes through an AA filter that could introduce an overall analog bandwidth limitation before sampling. Finally, the sampled sequence is handled by an equivalent equalization stage that models the DSP action of the transceiver. This abstraction captures the dominant effects of noise, electrical filtering, and digital compensation while avoiding the complexity of the full schematic.

As a first approximation, the equivalent transceiver noise can be modeled as white, and the AA filter can be modeled as sufficiently broad so that no additional filtering effect is applied at the receiver stage. For some commercial transceivers, it may be necessary to account for electrical filtering and colored noise in the receiver model, as will be discussed in later sections. In this section, we assess the transceiver performance for Vendors A and B using a fitting formula for their equivalent SNR. The result of this procedure is provided in Figure 4.

The bit error rate is expressed as:

$$\mathrm{BER} = k_1 \cdot \mathrm{erfc}\left(\sqrt{k_2 \cdot \mathrm{SNR}}\right) \tag{3}$$

where k_1 and k_2 depend on the modulation format [16], [21] and are reported in Table 1. The analytical models considered in this work provide an effective post-equalization SNR, where residual linear distortion and enhanced colored noise are included in the equalization error variance. Therefore, the BER mapping in (3) is used as an AWGN-equivalent approximation, whose validity is assessed experimentally. Under severe asymmetric filtering, especially for DP-16QAM, residual intersymbol interference (ISI) may cause deviations from this approximation; this discrepancy is accounted for in the error analysis rather than hidden by re-fitting the model.

The total system SNR is obtained using the Gaussian channel model, which has been shown to apply to metro-access network scenarios in [22], as the inverse sum of the individual contributions:

$$\mathrm{SNR}^{-1} = \mathrm{SNR}_{\mathrm{ASE}}^{-1} + \mathrm{SNR}_{\mathrm{TRX}}^{-1} \tag{4}$$

where the ASE-related contribution is defined in terms of the received optical power (ROP) as

$$\mathrm{SNR}_{\mathrm{ASE}} = \left.\frac{\mathrm{ROP}}{P_{\mathrm{ASE}}}\right|_{Bw=R_s} \tag{5}$$

where P_{ASE} is the total ASE-noise power injected into the optical link. The only impairment in the optical domain (other than filtering, which will be taken into account later on) is ASE noise, because we neglect the fiber nonlinearity. Moreover, we take the symbol rate as a reference bandwidth to compute the noise power. The transceiver contribution is further decomposed into transmitter (TX) and receiver (RX) components:

$$\mathrm{SNR}_{\mathrm{TRX}}^{-1} = \mathrm{SNR}_{\mathrm{TX}}^{-1} + \mathrm{SNR}_{\mathrm{RX}}^{-1} \tag{6}$$

The transmitter impact is considered constant due to fixed output power (typical values range from -10 dBm to 1 dBm), and it is assumed to have a negligible impact compared with that of the receiver. The receiver contribution varies with the ROP, primarily due to photodetector noise sources including thermal, shot, and dark current noise.

To model transceiver performance, the effective transceiver $\mathrm{SNR}_{\mathrm{TRX}}$ is determined through simplified curve fitting based on experimental data and the equation and procedure proposed in [8] and [9]. The formula, in linear scale, follows:

$$\mathrm{SNR}_{\mathrm{TRX}} = N \cdot \frac{\mathrm{ROP}}{\mathrm{ROP} + D} \tag{7}$$

where ROP is expressed in mW and N and D are two fitting parameters to obtain the dashed line in Figure 4. To plot the back-to-back characterization, conversion to dB scale was performed on ROP and $\mathrm{SNR}_{\mathrm{TRX}}$ for better visualization.

As reported in Table 1, both transceivers operate at the same symbol rate for DP-QPSK 200G and DP-16QAM 400G modulation formats. Since the internal noise contributions of the device are independent of the modulation format, the fitting parameters N and D can be assumed to be the same for both cases and are therefore fitted simultaneously in Figure 4. This property is particularly advantageous given the different characteristics of the two modulation formats. In particular, DP-QPSK is more robust and can therefore be used to characterize the device under low-ROP conditions. Conversely, DP-16QAM is more suitable at high ROP values, where DP-QPSK yields extremely low BER levels. In such conditions,

BER measurements with DP-QPSK become inaccurate and tend to saturate between BER = 10^{-10} and BER = 10^{-9} since typically in commercial transceivers BER estimation is performed only on the overhead bits. The saturation is depicted with empty bullets in Figure 4.

The experimental setup to obtain the curves of Figure 4 was prepared by excluding external noise sources in a back-to-back transceiver connection whose signal can be attenuated using a variable optical attenuator (VOA). By changing the attenuation we tested different ROP conditions, enabling the generation of $\mathrm{SNR}_{\mathrm{TRX}}$(ROP) curves by mapping BER measurements to SNR values through inversion of (3) with the proper modulation format coefficients $k_{1,2}$, remembering that for this characterization, $\mathrm{SNR}_{\mathrm{TRX}}$ is the only relevant SNR contribution. The resulting curves demonstrate monotonic SNR growth towards saturation at high ROP.

C. LITERATURE REVIEW

Bandwidth-limited channels and equalization are well established in wireless communications [29], [30], [31] and form the basis of the proposed models. Their application to optical systems, however, requires adaptations. First, the optical channel transfer function, intended as the physical-medium response and not as a wavelength-division-multiplexing (WDM) channel, can be accurately characterized and modeled, as shown in Section III-A. Second, alternating amplification and filtering in optical devices such as ROADMs causes distributed AWGN injection along the lightpath. Since each noise contribution undergoes different filtering from the transmitted signal, the resulting noise is colored and must be included in the model.

Filtering penalties in optical networks have been experimentally investigated in several works. In [32], filtering-penalty characterization and mitigation in meshed optical networks with a large number of ROADMs were demonstrated using optical wave shapers. Experiments in a metro-access scenario with a single ROADM and a single noise source were reported in [33]. The impact of optical-filter frequency shift and bandwidth variation on the Q-factor was analyzed through experiments and simulations in [34], highlighting the relevance of asymmetric filtering.

Several analytical models have also been proposed. In [23], performance degradation due to in-line optical filtering by wavelength-routing nodes in WDM networks is modeled using the digital communication theory of band-limited channels with linear equalization and validated experimentally with a commercial transponder and nonlinear fiber transmission. Continuous-time equalization is also considered in [24], where the model is validated with a single ROADM and a single ASE noise source, including optical-filter bandwidth variation and central-frequency shift. This work is extended in [25] to cascaded WSSs and to a fully coherent converged metro-access scenario, including a statistical analysis of central-frequency misalignment.

Discrete-time approaches have been proposed in [26] and [35]. In [26], an MMSEE equalization model based on the discrete-time Fourier transform (DTFT) is introduced, emphasizing the role of the relative placement of ASE noise sources and filters, as well as the implementation-dependent capabilities of the DSP receiver. Bandwidth variation is also considered, and validation is performed through time-domain simulations. In [35], a DTFT-based FSE model is adopted to perform a statistical analysis of filtering penalties under random WSS central-frequency and bandwidth variations. These quantities are modeled as Gaussian random variables according to [36]. The results show that both central-frequency and bandwidth misalignments must be considered to obtain conservative and reliable margins in the presence of filtering effects.

Finite-tap equalization has been addressed through two main approaches. In [27], noise whitening is applied before sampling and equalization, leading to a matrix-based semi-analytical WFLE model. Although this introduces approximations in a finite-length framework, good prediction accuracy is reported through time-domain simulations. A second, more realistic approach avoids noise whitening before sampling, which we refer to as FLE. A preliminary matrix-based semi-analytical model was presented in [28] and validated through time-domain simulations. The finite-tap equalizer model without whitening filtering was later analyzed and validated in [20], with a focus on finite-length equalization in filtering-limited coherent systems and on metro-access and passive-optical-network (PON)-motivated operating regimes, adopting receiver sensitivity, power penalty, required optical signal-to-noise ratio (ROSNR) penalty, and equalizer-output SNR as the main QoT metrics. In that work, the power spectral density (PSD) of the transceiver is defined according to [37], resulting in a non-generic spectral shape.

In this work, both WFLE and FLE are considered and compared, and the limitations of the whitening assumption are discussed. To the best of our knowledge, this comparison is presented here for the first time. Moreover, both WFLE and FLE are generalized to an arbitrary transceiver-noise PSD, and the evaluation is kept suitable for ONDT development by adopting generic performance metrics rather than PON-specific ones. The comparison in Table 2 summarizes these distinctions and illustrates the positioning of this work within the existing literature on filtering-penalty modeling.

In parallel, increasing attention has been devoted to the convergence of metro and access networks, where heterogeneous services, variable symbol rates, and dynamic routing lead to highly variable filtering conditions [1], [22], [38]. In this context, filtering penalties have been shown to strongly interact with transceiver impairments and receiver DSP capabilities [10], [25], [33]. Therefore, filtering effects cannot be treated as static margins, but must be dynamically evaluated as a function of network configuration, transceiver operating point, and noise distribution.

This aspect is closely related to the development of ONDTs. Recent advances in physical-layer digital-twin modeling have enabled accurate representations of fiber

TABLE 2. Comparison between the proposed framework and previous peer-reviewed works on filtering-penalty modeling and validation. ✓: included; ○: partially included or subject to restrictive assumptions;–: not addressed. AA: anti-aliasing; CD: chromatic dispersion; MIMO: multiple-input multiple-output; O/E: optical-to-electrical; OSNR: optical signal-to-noise ratio; PDL: polarization-dependent loss; PMD: polarization-mode dispersion; MMSE: minimum mean-square error; SDM: space-division multiplexing; TRX: transceiver.

Work	Distributed ASE	TRX-noise model	AA filtering	Equalizer models	Multi-span commercial validation	ONDT-oriented analysis	Main scope / limitation
[10]	✓	ROP-dependent AWGN	–	ZFE	✓	○	Measurement-oriented TRX/filtering model for converged metro-access links. It does not include finite-length equalization or arbitrary colored TRX-noise PSDs.
[18]	✓	AWGN	✓	MIMO FLE	–	–	Finite-length non-integer MIMO MMSE model including filtering, CD, PMD, PDL, distributed colored ASE, and receiver filtering. No arbitrary calibrated TRX-noise PSD or commercial validation.
[20]	✓	Fixed PSD	✓	FLE	○	–	Semi-analytical finite-length MMSE model with filtering, colored noise, and experimental verification. TRX noise uses a fixed PSD model; no WFLE/FLE comparison or arbitrary TRX-noise PSD. Experiments consider single span.
[23]	✓	AWGN	–	MMSEE	✓	–	In-line filtering model based on infinite-length MMSE equalization, validated with a commercial transponder. No characterized TRX-noise PSD, AA filtering, or finite-tap DSP.
[24]	–	ROP-dependent AWGN	–	MMSEE	○	–	Filtering-power-penalty model with lumped ASE and receiver noise, validated over OSNR/ROP variations. No distributed ASE or finite-tap equalization; experiments consider only single span.
[25]	○	AWGN	✓	MMSEE	○	–	Commercial filtering characterization with measured spectra and receiver electrical filtering. The analytical model assumes infinite-length MMSE; experiments consider only single span.
[26]	–	AWGN	–	MMSEE	○	○	Study of single-/double-sided filtering, ASE/filter placement, and DSP-dependent effects. The analytical model is discrete-time Fourier transform (DTFT)-based and infinite-length; no finite taps or arbitrary TRX-noise PSD.
[27]	○	AWGN	–	MIMO WFLE	–	–	Complexity-aware finite-length MIMO framework for SDM systems with linear impairments, filtering, and colored noise. Not focused on scalar WSS penalties or commercial TRX characterization.
[28]	✓	–	–	FLE	–	–	Matrix-based finite-length MMSE model for filtering with distributed ASE, validated by simulations. It assumes ideal O/E conversion and excludes TRX noise, AA filtering, and commercial validation.
This work	✓	Arbitrary PSD	✓	ZFE, MMSEE, FSE, WFLE, FLE	✓	✓	Unified scalar-amplitude filtering framework with distributed ASE, receiver-side TRX noise, arbitrary normalized TRX-noise PSD, AA filtering, finite-length equalization, simulations, and calibrated commercial validation. CD, phase effects, PMD, and PDL are outside scope.

propagation and optical amplification [5], often based on Gaussian-channel approximations [6]. Although these frameworks provide reliable estimates of nonlinear interference and ASE noise, the inclusion of filtering penalties remains an open issue. Existing ONDT models typically rely on coarse penalties or empirical margins [39], which may limit their accuracy in disaggregated and open optical networks, where filtering conditions are highly variable [4], [40]. This work addresses this gap by proposing an analytical framework for filtering-penalty evaluation designed for integration into digital-twin architectures. Equalization is modeled in both continuous and discrete time and validated through simulations. Multiple strategies are compared, including ZFE, MMSEE, FSE, WFLE, and FLE.

II. MODELS

In this section, we present a comprehensive framework for equalization models tailored to the specific requirements and characteristics of optical communication systems discussed in Sections I-A.

We consider both infinite- and finite-length equalizers and introduce a unified formalism for their implementation that encompasses the various abstractions proposed in the literature. Beyond reviewing these models, we generalize them to the case of arbitrary transceiver-noise PSD, with the goal of providing a rigorous and practically relevant tool for ONDT implementation.

For each model, we highlight its main strengths, limitations, and simplifying assumptions, in order to clarify when a given abstraction should be preferred and how the appropriate level of complexity can be selected according to the target application, since in many cases a simpler model may provide sufficient accuracy without requiring a more realistic and computationally demanding description. Throughout the paper, $(\cdot)^T$ denotes transpose, $(\cdot)^*$ denotes element-wise complex conjugation, and $(\cdot)^\dagger$ denotes the Hermitian transpose, i.e., the conjugate transpose.

A. OPTICAL LINK ABSTRACTION

The starting point for the analytical determination of the filtering penalty in optical systems is the block diagram shown in Figure 5. A general optical link is represented. We consider dual-polarization coherent transmission and focus on evaluating the SNR for the symbol sequence transmitted through one of the two polarizations. This approach is justified, since the filtering effect acts identically on both polarizations. Therefore, when computing the total SNR as the average of the SNR on the two polarizations, we obtain the same result. In addition, we assume that the modulation uses in-phase and quadrature components, as is done in modern optical transceivers.

For each polarization, the transmitted symbols are $\{x_k\}_{k=0}^{K-1}$ over K successive symbol intervals and are generated at the

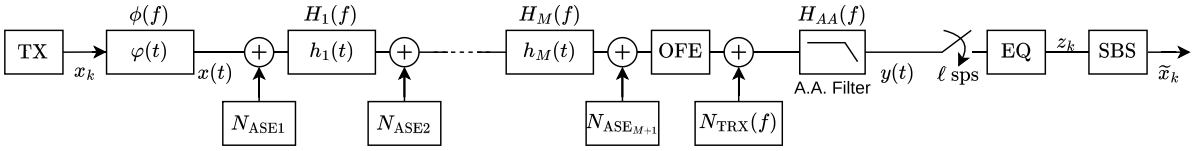

FIGURE 5. Reference optical link abstraction for the derivation of the equalization models.

symbol rate R_s. Denoting the symbol period by $T = 1/R_s$, the symbol energy is

$$\mathcal{E}_x = \mathbb{E}\left[|x_k|^2\right] \tag{8}$$

Consequently, the total transmitted signal power, accounting for both polarizations, is computed as follows:

$$P_{\mathrm{TX}} = 2 \cdot \frac{\mathcal{E}_x}{T} = 2 \cdot \mathcal{E}_x \cdot R_s \tag{9}$$

For derivation purposes, it is also useful to define the per-dimension energy, namely the energy of the in-phase or quadrature component of one polarization:

$$\bar{\mathcal{E}}_x = \frac{1}{2}\mathcal{E}_x = \frac{P_{\mathrm{TX}}}{4 \cdot R_s} \tag{10}$$

The x_k symbols are modulated by the shaping filter $\varphi(t)$ (assumed to satisfy the Nyquist criterion for intersymbol-interference-free channels and symbol-by-symbol (SBS) detection, and with Fourier transform $\Phi(f) = \mathcal{F}[\varphi(t)]$), so we can write the modulator output.

$$x(t) = \sum_{k=0}^{K-1} x_k \cdot \varphi(t - kT) \tag{11}$$

The modulated symbols pass through a cascade of M optical filters described by their transfer functions $H_i(f)$ $(i = 1, \ldots, M)$ experiencing the injection of distributed noise along the line, before the AA filter $H_{AA}(f)$. The signal is then sampled at ℓ samples per symbol (in commercial transceivers typically $\ell = 2$). After sampling, the signal is equalized, and SBS detection is performed on the z_k $(k = 0, \ldots, K-1)$ outputs of the equalizer, providing the final estimates $\hat{x}_k$ of the input symbols.

This model incorporates some simplifying assumptions. As anticipated in the previous section, we can assume the absence of the NLI, because metro and access networks are characterized by short links and low optical power [2]. Nevertheless, as proposed in [22], NLI can be conservatively accounted for if included as a Gaussian noise source concentrated on the receiver side.

All the ASE noise sources are assumed to be characterized by a flat PSD with a value of $N_{\mathrm{ASE,i}}$ (where $i = 1, \ldots, M+1$) for each ASE source, at least within the signal bandwidth. Therefore, each ASE contribution is an additive white Gaussian-noise source when injected into the link. The PSD of ASE noise due to optical amplification can be computed using the well-known formula [41].

$$N_{\mathrm{ASE}_i} = \frac{1}{4} \sum_{j=1}^{L_i} h f_0 (G_{j,i} - 1) NF_{j,i} \tag{12}$$

where L_i is the number of amplified spans located between each pair of optical filters, h is Planck's constant, f_0 is the central frequency of the transmitted signal, and $G_{j,i}$ and $NF_{j,i}$ are the gain and noise figure (NF), respectively, of each amplifier. The factor $\frac{1}{4}$ is needed because the noise PSD is referred to each modulation component (in-phase or quadrature) and each polarization.

According to the transceiver model introduced in Section I-B, and represented in Figure 3, we consider the transceiver noise to incorporate the OFE impairments and to be concentrated at the receiver side, with a PSD assuming a generic shape $N_{\mathrm{TRX}}(f)$, which models the noise added for each component and polarization axis.

$$N_{\mathrm{TRX}}(f) = \dot{N}_{\mathrm{TRX}} \cdot S_{\mathrm{TRX}}(f) \tag{13}$$

where $\dot{N}_{\mathrm{TRX}}$ is the white-noise equivalent PSD value, expressed in mW/Hz, and $S_{\mathrm{TRX}}(f)$ is the dimensionless shape of the colored PSD, which we assume to be normalized so that

$$\frac{1}{R_s} \int_{-\frac{R_s}{2}}^{\frac{R_s}{2}} S_{\mathrm{TRX}}(f) df = 1 \tag{14}$$

Both $\dot{N}_{\mathrm{TRX}}$ and $S_{\mathrm{TRX}}(f)$ depend on $\mathrm{SNR}_{\mathrm{TRX}}$ and on the specific commercial transceiver under analysis. In the experimental validation in Section III-C.2, we provide a heuristic approach for selecting these parameters, while emphasizing that the ground truth of the transceiver PSD is often unavailable. If the PSD of the transceiver noise is assumed to be white, one can simply set $S_{\mathrm{TRX}}(f) = 1$ and compute $\dot{N}_{\mathrm{TRX}}$ as follows.

$$\dot{N}_{\mathrm{TRX}} = \frac{\mathrm{ROP}}{4 \cdot R_s \cdot \mathrm{SNR}_{\mathrm{TRX}}} \tag{15}$$

B. PSD AND SNR CONVENTIONS

All PSDs used in this work are two-sided baseband PSDs referred to one real modulation dimension, i.e., one quadrature of one polarization. The term baseband specifies that the spectra are referred to the equivalent receiver-side I/Q representation after coherent detection, rather than to the optical passband around the carrier frequency. The PSDs are therefore real-valued and non-negative quantities.

With this convention, the total dual-polarization signal power is obtained by summing over two polarizations and two quadratures. The quantity $\mathcal{E}_x = \mathbb{E}[|x_k|^2]$ denotes the energy per complex symbol on one polarization, while $\bar{\mathcal{E}}_x = \mathcal{E}_x/2$ is the energy per real modulation dimension. The ROP denotes the total dual-polarization signal power at the receiver reference point. Consequently, in the unfiltered reference case:

$$\mathrm{ROP} = 4 \cdot \bar{\mathcal{E}}_x \cdot R_s \tag{16}$$

TABLE 3. PSD and SNR normalization conventions adopted in this work. Noise PSDs are two-sided baseband PSDs referred to one real modulation dimension, i.e., one quadrature of one polarization.

Quantity	Definition and convention	Units
ROP	Total dual-polarization received optical power, including both quadratures.	mW
$\mathcal{E}_x$	Complex-symbol energy on one polarization, $\mathcal{E}_x = \mathbb{E}[\lvert x_k\rvert^2]$.	mW s
$\bar{\mathcal{E}}_x$	Energy per real modulation dimension, $\bar{\mathcal{E}}_x = \mathcal{E}_x/2$.	mW s
$N_{\mathrm{ASE},i}$	ASE-noise PSD of the i-th source, per real dimension.	mW/Hz
$\dot{N}_{\mathrm{TRX}}$	White-noise-equivalent transceiver-noise PSD, per real dimension.	mW/Hz
$S_{\mathrm{TRX}}(f)$	Dimensionless TRX-noise spectral shape, normalized as $\frac{1}{R_s}\int_{-R_s/2}^{R_s/2} S_{\mathrm{TRX}}(f)\,df = 1$.	–
$N_{\mathrm{TRX}}(f)$	Colored TRX-noise PSD, $N_{\mathrm{TRX}}(f) = \dot{N}_{\mathrm{TRX}} S_{\mathrm{TRX}}(f)$, per real dimension.	mW/Hz

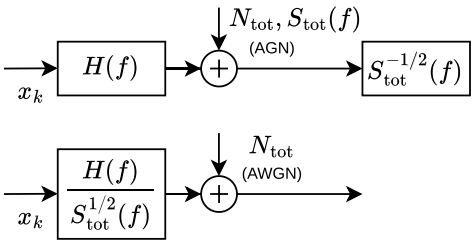

FIGURE 6. Noise-whitening scheme. AGN: additive Gaussian noise; AWGN: additive white Gaussian noise.

The same four-dimensional accounting is used for noise powers. In particular, the factor $1/4$ in the ASE PSD definition in (12) converts the total dual-polarization ASE contribution into the two-sided PSD referred to one real modulation dimension. Similarly, the white-noise-equivalent transceiver PSD in (15) is obtained by referring the transceiver-noise power to one quadrature of one polarization. All SNR- and PSD-related quantities are summarized in Table 3.

C. NOISE WHITENING

In Figure 5, the filtering stages make the total noise PSD at the receiver colored. In this case, a noise-whitening approach is widely used in digital communications to simplify the models. Exploiting the white-noise equivalent channel representation it is possible to derive without loss of information the ZFE, MMSEE, and FSE models with a uniform and elegant mathematical framework. In the following sections, we will also consider the WFLE, based on noise whitening, which is a reliable approximation already successfully exploited in past works [7], [27].

Figure 6 illustrates how to obtain a white-noise equivalent channel model, given the condition that the colored noise PSD has an invertible square root [29], [30]. In this section we derive the quantities $H(f)$, $S_{\mathrm{tot}}(f)$ and N_{tot}, which are the white-noise equivalent channel frequency response, the normalized colored noise PSD, and the white equivalent PSD, respectively. The initial step involves evaluating the noise on the receiver side, which is the sum of multiple components colored on the basis of the number and shape of crossed filters. Using the well-known formula to calculate the output PSD of a random process crossing a filter, knowing the input PSD we derive the normalized colored PSD before sampling:

$$S_{\mathrm{tot}}(f) = \frac{\sum_{i=1}^{M+1} N_{ASE,i} \prod_{n=i}^{M} |H_n(f)|^2 |H_{AA}(f)|^2}{N_{\mathrm{tot}}} + \frac{(\dot{N}_{\mathrm{TRX}} S_{\mathrm{TRX}}(f)) |H_{AA}(f)|^2}{N_{\mathrm{tot}}} \tag{17}$$

where $\prod_{n=M+1}^{M} |H_n(f)|^2 = 1$, the PSD of the transceiver noise is taken from (13), and the total colored noise PSD has been normalized by the following factor.

$$N_{\mathrm{tot}} = \sum_{i=1}^{M+1} N_{ASE,i} + \dot{N}_{\mathrm{TRX}} \tag{18}$$

Since the penalty on the link is due to linear filtering, the colored PSD expressed by (17) has an invertible square root. Moreover, due to the normalization factor, the PSD of the equivalent white noise source on the receiver side is N_{tot}.

Following the notation of [30], we introduce the white-noise equivalent pulse response of the optical link as the inverse Fourier transform of the white-noise equivalent channel frequency response.

$$h(t) = \mathcal{F}^{-1}[H(f)] \tag{19}$$

$$H(f) = \frac{\Phi(f) \cdot \prod_{i=1}^{M} |H_i(f)| |H_{AA}(f)|}{\sqrt{S_{\mathrm{tot}}(f)}} \tag{20}$$

where the numerator in (20) has been obtained from the cascade of the shaping filter, optical filters, and AA filter, with $\Phi(f)$ being the Fourier transform of the pulse response of the shaping filter. The denominator is due to the effect of the whitening filter according to Figure 6. The cancellation of $H_{\mathrm{AA}}(f)$ in the whitened equivalent channel must be interpreted under the ideal assumptions of continuous-time noise whitening, no aliasing, and an AA response that is common to the signal and to all receiver-side noise contributions. Under these assumptions, the whitened infinite-length models do not explicitly quantify the finite-memory penalty introduced by the electrical AA filter. This is no longer true for the following non-whitened FLE model, where $H_{\mathrm{AA}}(f)$ enters the sampled signal matrix and the sampled colored-noise covariance matrices before equalization. Therefore, electrical bandwidth limitation is physically relevant in the FLE formulation, while the whitened models should be interpreted as reference approximations.

Since the pulse energy is not necessarily normalized to 1, it is useful to introduce the normalized pulse response as follows.

$$\varphi_h(t) \triangleq \frac{h(t)}{\|h\|} \tag{21}$$

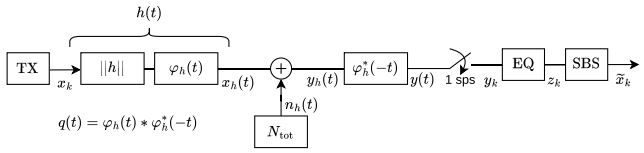

FIGURE 7. Reference block diagram for zero-forcing and minimum mean-square error equalizers with whitened noise.

where

$$\|h\| = \sqrt{\int_{-\infty}^{\infty} h(t) \cdot h^*(t) dt} = \sqrt{\langle h(t), h(t) \rangle} \tag{22}$$

so that the band limited channel output before noise injection is as follows.

$$x_h(t) = \sum_{k=0}^{K-1} x_k \cdot \|h\| \cdot \varphi_h(t - kT) \tag{23}$$

D. THE UNFILTERED SNR BOUND

In the optical system under study, the passband effect of the optical filters limits the channel, causing ISI that affects the performance in terms of SNR degradation. The maximum SNR is obtained when the filtering effect is negligible and therefore when the signal is not distorted. Such a situation can occur when the band of the filters is large compared to the signal bandwidth. When this happens, the SNR computation is straightforward, because ASE noise is flat in the signal bandwidth. We conclude that in this case the SNR computed taking into account ASE noise and transceiver noise, neglecting NLI, is as follows.

$$\mathrm{SNR}_{\max} = \left(\mathrm{SNR}_{\mathrm{ASE}}^{-1} + \mathrm{SNR}_{\mathrm{TRX}}^{-1}\right)^{-1} = \mathrm{SNR} \tag{24}$$

where $\mathrm{SNR}_{\mathrm{TRX}}$ is given in Section I-B. Since the signal and noise power can be computed, we can explicitly express the SNR bound according to the notation developed for noise whitening in Section II-C, which will be useful when deriving most of the considered equalization models, allowing their performance to be compared.

$$\mathrm{SNR} = \frac{\mathrm{ROP}}{P_{\mathrm{ASE}} + P_{\mathrm{TRX}}} = \frac{4 \cdot \bar{\mathcal{E}}_x \cdot R_s \cdot \|h\|^2}{4 \cdot N_{\mathrm{tot}} \cdot R_s} = \frac{\bar{\mathcal{E}}_x \cdot \|h\|^2}{N_{\mathrm{tot}}} \tag{25}$$

where we point out that bandwidth terms cancel out since both signal and noise power are computed with respect to the same band equal to the symbol rate.

E. INFINITE-LENGTH EQUALIZERS

In this section, we examine the infinite-length equalization models, namely the ZFE, MMSEE, and FSE. For the ZFE and MMSEE, additional assumptions and definitions are needed because these models are based on matched-filter theory. The optical link in Figure 7 represents the white-noise equivalent link for ZFE and MMSEE equalization. After matched filtering, the DSP is assumed to perform equalization operating at a sampling rate equal to 1 sample per symbol. The matched filtering assumption is not realistic in optical systems. In general, the presence of a matched filter before sampling is not necessary, since modern commercial transceivers implement both matched filtering and equalization in the discrete domain. This matched-filter assumption is removed when considering the FSE, WFLE, and FLE models.

We define the deterministic autocorrelation function $q(t)$ as follows.

$$q(t) \triangleq \varphi_h(t) * \varphi_h^*(-t) = \frac{h(t) * h^*(-t)}{\|h\|^2} \tag{26}$$

where the binary operator $*$ denotes convolution, whereas the superscript $(\cdot)^*$ denotes complex conjugation, as specified above. It is useful to note that $q(t)$ is Hermitian ($q(t) = q^*(-t)$) and that $q(0) = 1$.

Since in the considered optical system we assume that we know the expression of each filter and each noise contribution, it is possible to rewrite $Q(f) = \mathcal{F}[q(t)]$ explicitly.

$$Q(f) = \frac{|H(f)|^2}{\|h\|^2} = \frac{\left|\Phi(f) \cdot \prod_{i=1}^{M} H_i(f) \cdot H_{\mathrm{AA}}(f)\right|^2}{\|h\|^2 \cdot S_{\mathrm{tot}}(f)} \tag{27}$$

Once the channel model has been established, it is possible to derive the filtering penalty model according to the chosen equalization strategy based on the steps followed in [30]. In the following, we provide the expression of the SNR after equalization and the filtering penalty coefficient for all the considered equalization strategies.

1) ZERO-FORCING EQUALIZER

The reference system for the current model is provided in Figure 7. ZFE is the simplest and most intuitive equalizer among the ones considered in this work. However, it is also the worst in terms of performance, due to its noise enhancement effect. Nevertheless, its model allows one to express the filtering penalty in a disaggregated manner, based on a cumulative metric [6], as will be clear in the following and as shown in [10]. This feature is pivotal when including the filtering penalty in an ONDT transmission model; therefore, the ZFE is included in the present discussion. Moreover, in many practical applications in which filtering and noise are limited, the performance assessment given by the ZFE is very accurate yet conservative, as quantitatively assessed in the simulations in Section III-B. Based on the derivation provided in [30], the output SNR of the ZFE, expressed as a degradation of the unfiltered SNR, is as follows.

$$\mathrm{SNR}_{\mathrm{ZFE}} = \frac{\mathrm{SNR}}{k_{\mathrm{ZFE}}} \tag{28}$$

The filtering penalty factor k_{ZFE} is obtained based on the following expression.

$$k_{\mathrm{ZFE}} = \frac{1}{R_s} \int_{-\frac{R_s}{2}}^{\frac{R_s}{2}} \frac{1}{Q\left(e^{-j\frac{2\pi f}{R_s}}\right)} df \tag{29}$$

where, compared with [30], we replaced the symbol period by the inverse of the symbol rate, $T = 1/R_s$, expressed the equations in terms of frequency f rather than angular frequency $\omega = 2\pi f$, and replaced the noise PSD by the quantity previously computed in (18), namely $\mathcal{N}_0/2 = N_{\mathrm{tot}}$.

The term $Q\left(e^{-j\frac{2\pi f}{R_s}}\right)$ is the folded spectrum of $Q(f)$ in (27); it is periodic with period R_s and can be written as

$$Q\left(e^{-j\frac{2\pi f}{R_s}}\right) = R_s \cdot \sum_{n=-\infty}^{\infty} Q\left(f + nR_s\right) \tag{30}$$

For practical implementations, one can compute $Q\left(e^{-j\frac{2\pi f}{R_s}}\right)$ based on (27) performing a periodic repetition in frequency or numerically by undersampling in the time domain.

The disaggregation of ZFE can be performed by considering each noise source characterized by $N_{ASE,i}$ $(i = 1, \ldots, M+1)$ and $N_{\mathrm{TRX}}(f)$ individually and computing the corresponding constant k_i through (29), with the other sources injecting no noise in order to evaluate the colored PSD of (17). The final formula for computing k_i follows.

$$k_{ASE,i} = \frac{1}{R_s}\int_{-\frac{R_s}{2}}^{\frac{R_s}{2}} \frac{\prod_{n=i}^{M}\left|H_n\left(e^{j\frac{2\pi f}{R_s}}\right)\right|^2}{\left|\Phi\left(e^{j\frac{2\pi f}{R_s}}\right)\right|^2 \prod_{m=1}^{M}\left|H_m\left(e^{j\frac{2\pi f}{R_s}}\right)\right|^2} df \tag{31}$$

$$k_{\mathrm{TRX}} = \frac{1}{R_s}\int_{-\frac{R_s}{2}}^{\frac{R_s}{2}} \frac{S_{\mathrm{TRX}}\left(e^{j\frac{2\pi f}{R_s}}\right)}{\left|\Phi\left(e^{j\frac{2\pi f}{R_s}}\right)\right|^2 \prod_{m=1}^{M}\left|H_m\left(e^{j\frac{2\pi f}{R_s}}\right)\right|^2} df \tag{32}$$

This closed-form disaggregated formulation is especially valuable for ONDTs, as it allows filtering penalties to be embedded directly into the transmission model in an interpretable and scalable way, preserving the contribution of the individual network elements and supporting impairment-aware performance prediction.

2) MINIMUM MEAN-SQUARE ERROR EQUALIZER

The MMSEE equalizer balances ISI reduction and noise enhancement. In this case, the reference system is the same as ZFE, reported in Figure 7. As mentioned in Section II-E1, it is possible to define a filtering-penalty coefficient k_{MMSEE} with respect to the unfiltered SNR bound.

$$\mathrm{SNR}_{\mathrm{MMSEE}} = \frac{\mathrm{SNR}}{k_{\mathrm{MMSEE}}} - 1 \tag{33}$$

where the term "−1" is needed to obtain the unbiased SNR, since the MMSEE equalizer is by definition biased [30]. The explicit expression for k_{MMSEE} is derived in [30]; here, we report the final result.

$$k_{\mathrm{MMSEE}} = \frac{1}{R_s}\int_{-\frac{R_s}{2}}^{\frac{R_s}{2}} \frac{1}{\left(Q\left(e^{-j\frac{2\pi f}{R_s}}\right) + \frac{1}{\mathrm{SNR}}\right)} df \tag{34}$$

where R_s is the symbol rate, $Q\left(e^{-j\frac{2\pi f}{R_s}}\right)$ is computed as in the ZFE case, and the additional positive term $\frac{1}{\mathrm{SNR}}$, depending on the unfiltered bound for the SNR, is the only difference compared to the ZFE. This term represents the ability of the MMSEE equalizer to balance ISI reduction and noise enhancement.

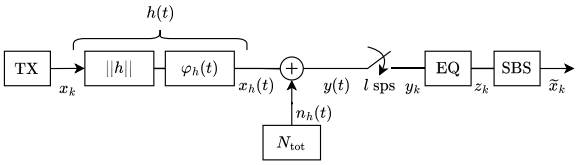

FIGURE 8. Reference block diagram for fractionally spaced and finite-length equalization with whitened noise.

3) FRACTIONALLY SPACED EQUALIZER

The reference channel-model block diagram for this section is provided in Figure 8. The FSE exploits the minimum mean-square error equalization strategy, with additional features that improve performance at a modest increase in complexity.

In this more realistic model, we eliminate the matched filter before sampling. The DSP performs both equalization and matched filtering in the discrete domain, according to what happens in commercial transceivers deployed in optical systems. In addition, the FSE increases the sampling rate by some rational number ℓ, $(\ell > 1)$, which we assume to be an integer. The unbiased SNR for the FSE is derived in [30], and the final expression is as follows.

$$\mathrm{SNR}_{\mathrm{MMSEE,FSE}} = \frac{\mathrm{SNR}}{k_{\mathrm{MMSEE,FSE}}} - 1 \tag{35}$$

The corresponding filtering penalty follows.

$$k_{\mathrm{MMSEE,FSE}} = \frac{1}{R_s}\int_{-\frac{R_s}{2}}^{\frac{R_s}{2}} \frac{\ell}{\left|\left|\mathbf{H}\left(e^{-j\frac{2\pi f}{R_s}}\right)\right|\right|^2 + \frac{\ell}{\mathrm{SNR}}} df \tag{36}$$

where the parameter $\left|\left|\mathbf{H}\left(e^{-j\frac{2\pi f}{R_s}}\right)\right|\right|^2$ accounts for the shape of the filters and for the PSD.

$$\left|\left|\mathbf{H}\left(e^{-j\frac{2\pi f}{R_s}}\right)\right|\right|^2 = \sum_{i=1}^{\ell}\left|H_i\left(e^{-j\frac{2\pi f}{R_s}}\right)\right|^2 \tag{37}$$

and it can be computed from the symbol-rate-spaced phases $H_i(D)$, evaluated in the unit circle. The expression of $H_i\left(e^{-j\frac{2\pi f}{R_s}}\right)$ is:

$$H_i\left(e^{-j\frac{2\pi f}{R_s}}\right) = \sum_{k=-\infty}^{\infty} h\left(kT - (i-1)\frac{T}{\ell}\right) \cdot D^k\Big|_{D=e^{-j\frac{2\pi f}{R_s}}} \tag{38}$$

For practical implementation purposes, we recall that the white-noise equivalent pulse response of the optical link $h(t)$ is defined in (19). Therefore, one can sample $h(t)$ to obtain the ℓ phases and then perform a Fourier transform to evaluate $H_i\left(e^{-j\frac{2\pi f}{R_s}}\right)$.

The structure of (36) is similar to the filtering-penalty coefficient of the MMSEE equalizer in (34). Indeed, the FSE is also based on the minimum mean-square error criterion and therefore can mitigate ISI while limiting noise enhancement. Moreover, practical adaptive implementations of the FSE based on the least-mean-squares (LMS) or constant-modulus algorithm (CMA) have been shown to converge to

MMSEE-equalizer performance [42]. In the present analysis, timing-related effects are not considered; therefore, the possible additional benefit of the FSE observed in practical implementations, in particular its improved robustness to sampling-phase errors [29], [30], is beyond the scope of this discussion.

F. FINITE-LENGTH EQUALIZERS

The models analyzed previously assume infinite-length filtering. In practical applications, the equalization filter is implemented as a finite-impulse-response (FIR) filter. This is because adaptive equalization techniques strongly exploit FIR structures. The models proposed in this section are based on MMSEE equalization.

1) WHITENED FINITE-LENGTH EQUALIZER

As done for the FSE case, the reference block scheme is depicted in Figure 8. At this stage, we keep the previously defined channel function $h(t)$ embedding the PSD of the colored noise, therefore, assuming whitening filtering, as done in [7], [27], and [30].

We recall that $\ell > 1$ is the oversampling factor. Therefore, after sampling at $t = kT - \frac{iT}{\ell}$ $(i = 0, \ldots, \ell - 1)$ the channel output becomes as follows.

$$y\left(kT - \frac{iT}{\ell}\right) = \sum_{m=-\infty}^{\infty} x_m \cdot h\left(kT - \frac{iT}{\ell} - mT\right) + n\left(kT - \frac{iT}{\ell}\right) \tag{39}$$

where the variance of the sampled noise, as for the FSE, is equal to $\ell \cdot N_{\text{tot}}$.

It is possible and convenient to represent the channel using vectors and matrices, by grouping the ℓ phases per symbol period of the oversampled $y(t)$.

$$\mathbf{y}_k = \sum_{m=-\infty}^{\infty} x_{k-m} \cdot \mathbf{h}_m + \mathbf{n}_k \tag{40}$$

where:

$$\begin{aligned} \mathbf{y}_k &= \left[y(kT),\, y\left(kT - \tfrac{T}{\ell}\right), \ldots y\left(kT - \tfrac{\ell-1}{\ell}T\right)\right]^T \\ \mathbf{h}_k &= \left[h(kT),\, h\left(kT - \tfrac{T}{\ell}\right), \ldots h\left(kT - \tfrac{\ell-1}{\ell}T\right)\right]^T \\ \mathbf{n}_k &= \left[n(kT),\, n\left(kT - \tfrac{T}{\ell}\right), \ldots n\left(kT - \tfrac{\ell-1}{\ell}T\right)\right]^T \end{aligned} \tag{41}$$

The analysis in this section is carried out in the time domain, based on some assumptions needed to describe the discretized channel in matrix form. The step-by-step derivation is provided in [30]. Here we report the main passages and considerations that are useful to understand the final expression.

The channel pulse response $h(t)$ is assumed to extend over a finite time interval, so any nonzero value of $h(t)$ is considered negligible outside of this interval, which is defined as $-(\ell - 1)T/\ell \leq t \leq \nu T$. Therefore, $\mathbf{h}_k \approx 0$ for $k < 0$ and $k > \nu$. If this does not happen, the model accuracy is reduced due to an arbitrary truncation of the channel. In most cases, it is possible to find the value of ν to avoid this approximation despite the fact that the whitening filter tends to create long temporal tails in $h(t)$. Further discussion on the limit of this model is provided in the next section, which focuses on the FLE mathematical model without the whitening filtering assumption. Moreover, a performance comparison is carried out in Section III-B. In this work, ν is not used as a fitting parameter nor investigated as an additional degree of freedom, since the focus is on the impact of filtering, distributed noise, transceiver impairments, and equalizer tap number on the filtering penalty. In the numerical implementation, ν is fixed equal to the number of symbols used to generate the sampled pulse responses. This provides a conservative truncation window for the construction of the finite-dimensional channel matrices that follows.

We consider that N_f successive ℓ-tuples of samples of $y(t)$ are exploited to perform equalization. The coefficient N_f is related to the number of taps of the FLE, which can be calculated from the product $\ell \cdot N_f$. The final assumption is that ℓ is an integer, which leads to a simpler expression for the channel matrix. Based on the previous assumptions, the channel model is as follows.

$$\begin{aligned} \mathbf{Y}_k = \left[\mathbf{y}_k, \mathbf{y}_{k-1}, \ldots \mathbf{y}_{k-N_f+1}\right]^T = \\ = \begin{bmatrix} \mathbf{h}_0 & \mathbf{h}_1 & \ldots & \mathbf{h}_\nu & 0 & 0 & \ldots & 0 \\ 0 & \mathbf{h}_0 & \mathbf{h}_1 & \ldots & \mathbf{h}_\nu & 0 & \ldots & 0 \\ \vdots & \vdots & \ddots & \ddots & \ddots & \ddots & \ddots & \vdots \\ 0 & \ldots & 0 & 0 & \mathbf{h}_0 & \mathbf{h}_1 & \ldots & \mathbf{h}_\nu \end{bmatrix} \cdot \\ \cdot \begin{bmatrix} x_k \\ x_{k-1} \\ \vdots \\ \vdots \\ x_{k-N_f-\nu+1} \end{bmatrix} + \begin{bmatrix} \mathbf{n}_k \\ \mathbf{n}_{k-1} \\ \vdots \\ \mathbf{n}_{k-N_f+1} \end{bmatrix} \end{aligned} \tag{42}$$

The $(N_f \cdot \ell) \times (N_f + \nu)$ matrix in (42) is denoted as $\mathbf{H}$, while the data vector and the noise vector are defined, respectively, as $\mathbf{X}_k$ and $\mathbf{N}_k$. Then the compact form of (42) becomes:

$$\mathbf{Y}_k = \mathbf{H} \cdot \mathbf{X}_k + \mathbf{N}_k \tag{43}$$

In addition to the noise variance information, $\mathbf{H}$ fully describes the filtering penalty for finite-length equalization. The equalizer processes the sampled output channel vector $\mathbf{Y}_k$ by taking the inner product of a row vector of equalizer coefficients having dimension $N_f \ell$. Therefore, the equalizer output samples z_k in Figure 5 are written as follows.

$$z_k = \mathbf{w} \cdot \mathbf{Y}_k \tag{44}$$

For a causal practical implementation, a channel-equalizer system delay $\Delta \cdot T$ symbol periods is selected.

$$\Delta \approx \frac{\nu + N_f}{2} \tag{45}$$

The exact value of Δ has a significant impact only if N_f is very low.

The WFLE unbiased SNR, with whitening filtering, is obtained as follows.

$$\mathrm{SNR}_{\mathrm{MMSEE,WFLE}} = \frac{\bar{\mathcal{E}}_x}{\sigma^2_{\mathrm{MMSEE,WFLE}}} - 1 \tag{46}$$

where the post-equalization noise variance is:

$$\sigma^2_{\mathrm{MMSEE,WFLE}} = \bar{\mathcal{E}}_{\mathbf{x}} - \mathbf{w} \cdot R_{\mathbf{YY}} \cdot \mathbf{w}^{\dagger} \tag{47}$$

The symbol † denotes the Hermitian transpose, i.e., the conjugate transpose.

The expression of the noise variance after the equalizer in (47) depends on the vector of the equalizer coefficients $\mathbf{w}$.

$$\mathbf{w} = R_{x\mathbf{Y}} \cdot R^{-1}_{\mathbf{YY}} \tag{48}$$

To express $\sigma^2_{\mathrm{MMSEE,WFLE}}$ and $\mathbf{w}$, it is necessary to compute the correlation matrices $R_{\mathbf{YY}}$ and $R_{x\mathbf{Y}}$, which are the autocorrelation matrix of the output samples and the cross-correlation matrix of the input-output samples, respectively. Both $R_{\mathbf{YY}}$ and $R_{x\mathbf{Y}}$ depend on the channel matrix $\mathbf{H}$ and the noise autocorrelation matrix $R_{\mathbf{NN}} = \ell \cdot N_{\mathrm{tot}} \cdot \mathbf{I}$. The noise autocorrelation matrix is diagonal since we consider whitened noise.

$$R_{\mathbf{YY}} = \bar{\mathcal{E}}_{\mathbf{x}} \cdot \mathbf{H}\mathbf{H}^{\dagger} + R_{\mathbf{NN}} \tag{49}$$

$$R_{x\mathbf{Y}} = \bar{\mathcal{E}}_{\mathbf{x}} \cdot [0 \ldots 0, \mathbf{h}^{\dagger}_{\nu} \ldots \mathbf{h}^{\dagger}_{0}, 0 \ldots 0] \tag{50}$$

where $R_{x\mathbf{Y}}$ is an $(N_f \cdot \ell)$-dimension row vector that depends on the choice of the delay factor Δ. Indeed, $R_{x\mathbf{Y}}$ can also be written as follows.

$$R_{x\mathbf{Y}} = \bar{\mathcal{E}}_{\mathbf{x}} \cdot \mathbf{1}^{\dagger}_{\Delta} \cdot \mathbf{H}^{\dagger} \tag{51}$$

where $\mathbf{1}_{\Delta}$ is an $(N_f + \nu)$-dimensional column vector of zeros with a one in the $(\Delta + 1)^{\mathrm{th}}$ position.

2) FINITE-LENGTH EQUALIZER

A more realistic FLE model can be obtained by considering the initial link abstraction, depicted in Figure 5, whose main features and assumptions were discussed in Section II-A. In this case, noise whitening is not applied before sampling. Then matched filtering and equalization are performed in discrete domain after oversampling by a factor ℓ.

As anticipated, the ideal noise whitening leads to an approximation of the WFLE performance. The continuous-time whitening filter $1/\sqrt{S_{\mathrm{tot}}}$ in (19) can have infinite pulse response. This creates long tails in the equivalent channel pulse response $h(t)$. In such cases, the assumption $h(t) \approx 0$ for $t \leq -(\ell - 1)T/\ell$ and $t \geq \nu T$ is not valid, causing a truncation of $h(t)$ when building the channel matrix $\mathbf{H}$ defined in (42) and (43). In addition, if no whitening is applied to the noise before sampling, the noise autocorrelation matrix $R_{\mathbf{NN}}$ in (49) is not diagonal and must be computed based on the pulse responses experienced by each noise source in the link.

We define the channel pulse response as follows.

$$\tilde{h}(t) = \mathcal{F}^{-1}\left[\Phi(f) \cdot \prod_{i=1}^{M} |H_i(f)| \cdot |H_{\mathrm{AA}}(f)|\right] \tag{52}$$

Notably, the colored PSD is not included in the channel pulse response expression. Each noise source is a continuous-time signal which is sampled at ℓ/R_s rate after the convolution with the filters. The channel pulse response for each ASE noise source is expressed as follows.

$$\tilde{g}_i(t) = \mathcal{F}^{-1}\left[\prod_{n=i}^{M} |H_n(f)| \cdot |H_{\mathrm{AA}}(f)|\right] \quad i = 1, \ldots, M+1 \tag{53}$$

where, as in (17), we assume $\prod_{n=M+1}^{M} |H_n(f)| = 1$.

Regarding the transceiver noise, it is necessary to consider the colored nature of the PSD that we are assuming, in addition to the AA filter.

$$\tilde{g}_{\mathrm{TRX}}(t) = \mathcal{F}^{-1}\left[\sqrt{S_{\mathrm{TRX}}(f)} \cdot |H_{\mathrm{AA}}(f)|\right] \tag{54}$$

As done in Section II-F.1 for the WFLE, it is convenient to group the ℓ phases per symbol period of the pulse response of the channel as follows.

$$\tilde{\mathbf{h}}_k = \left[\tilde{h}(kT)\ \tilde{h}\left(kT - \tfrac{T}{\ell}\right) \ldots \tilde{h}\left(kT - \tfrac{(\ell-1)}{\ell}T\right)\right]^T \tag{55}$$

To build finite-dimensional matrices we also consider in this case that we collect the samples of $\tilde{h}(t)$ and $\tilde{g}_i(t)$ according to the factor ν in the time interval $-(\ell - 1)T/\ell \leq t \leq \nu T$. As stated at the beginning of this section, the absence of the whitening filter leads to higher accuracy than the WFLE. Without the whitening filter, the truncation of the time interval is expected to be much more accurate due to the fact that $\tilde{h}(t)$ and $\tilde{g}_i(t)$ are expected to be finite pulse responses.

Based on the pulse response vectors defined in (55) and the pulse responses in (53), it is possible to rewrite the autocorrelation matrix of the output samples and the cross-correlation matrix of the input-output samples of (49) and (50) as follows [20].

$$\tilde{R}_{\mathbf{YY}} = \bar{\mathcal{E}}_{\mathbf{x}} \widetilde{\mathbf{H}} \widetilde{\mathbf{H}}^{\dagger} + \sum_{i=1}^{M+1} N_{ASE,i} \widetilde{\mathbf{G}}_i \widetilde{\mathbf{G}}_i^{\dagger} + \dot{N}_{\mathrm{TRX}} \widetilde{\mathbf{G}}_{\mathrm{TRX}} \widetilde{\mathbf{G}}^{\dagger}_{\mathrm{TRX}} \tag{56}$$

$$\tilde{R}_{x\mathbf{Y}} = \bar{\mathcal{E}}_{\mathbf{x}} \cdot [0 \ldots 0, \tilde{\mathbf{h}}^{\dagger}_{\nu} \ldots \tilde{\mathbf{h}}^{\dagger}_{0}, 0 \ldots 0] \tag{57}$$

The products $\widetilde{\mathbf{G}}_i \widetilde{\mathbf{G}}_i^{\dagger}$ and $\widetilde{\mathbf{G}}_{\mathrm{TRX}} \widetilde{\mathbf{G}}^{\dagger}_{\mathrm{TRX}}$ represent the discrete-time covariance kernels of the filtered continuous-time noise sources after sampling at ℓ samples per symbol. The sampling-interval normalization associated with the discretization is included in the sampled pulse responses used to build $\widetilde{\mathbf{G}}_i$ and $\widetilde{\mathbf{G}}_{\mathrm{TRX}}$. Therefore, no additional sampling factor appears explicitly in (56).

In (56) $\widetilde{\mathbf{H}}$ shares structural similarities with the channel matrix $\mathbf{H}$ defined in (42) and (43), being a $(N_f \cdot \ell) \times (N_f + \nu)$ Toeplitz matrix, which can be built from $\tilde{h}(t)$ as follows.

$$\widetilde{\mathbf{H}} = \begin{bmatrix} \tilde{\mathbf{h}}_0 & \tilde{\mathbf{h}}_1 & \ldots & \tilde{\mathbf{h}}_{\nu} & 0 & 0 & \ldots & 0 \\ 0 & \tilde{\mathbf{h}}_0 & \tilde{\mathbf{h}}_1 & \ldots & \tilde{\mathbf{h}}_{\nu} & 0 & \ldots & 0 \\ \vdots & \vdots & \ddots & \ddots & \ddots & \ddots & \ddots & \vdots \\ 0 & \ldots & 0 & 0 & \tilde{\mathbf{h}}_0 & \tilde{\mathbf{h}}_1 & \ldots & \tilde{\mathbf{h}}_{\nu} \end{bmatrix} \tag{58}$$

In (56) we also defined the matrices $\widetilde{\mathbf{G}}_i$ for $i = 1, \ldots, M + 1$, which represent the channel matrix for each ASE noise

source and are built starting from the pulse responses defined in (53) as follows.

$$\dot{g}_{i,k,j} \triangleq \tilde{g}_i\left(kT - j\frac{T}{\ell}\right), \quad k = 0,\ldots,\nu; \quad j = 0,\ldots,\ell-1$$

$$\widetilde{\mathbf{G}}_i = \begin{bmatrix} \dot{g}_{i,0,\ell-1} & \dot{g}_{i,0,\ell-2} & \cdots & \dot{g}_{i,\nu,0} & 0 & 0 & \cdots & 0 \\ 0 & \dot{g}_{i,0,\ell-1} & \dot{g}_{i,0,\ell-2} & \cdots & \dot{g}_{i,\nu,0} & 0 & \cdots & 0 \\ \vdots & \ddots & \ddots & \ddots & & \ddots & \ddots & \\ 0 & \cdots & 0 & 0 & \dot{g}_{i,0,\ell-1} & \dot{g}_{i,0,\ell-2} & \cdots & \dot{g}_{i,\nu,0} \end{bmatrix} \tag{59}$$

Notably, $\widetilde{\mathbf{G}}_i$ are $(N_f \cdot \ell) \times ((N_f + \nu + 1) \cdot \ell - 1)$ Toeplitz matrices, with a quite different structure compared to $\widetilde{\mathbf{H}}$. The reason is that, differently from the signal that is generated at the symbol rate, the noise terms are continuous-time sources sampled at ℓ times the symbol rate after the convolution with the pulse responses of the filters. Therefore, for the noise sources, it is not possible to group the ℓ phases per symbol period, as is done to represent the convolution between $\tilde{h}(t)$ and the transmitted symbols x_k. Regarding the transceiver noise, $\widetilde{\mathbf{G}}_{\mathrm{TRX}}$ has the same structure shown in (59), but considering the pulse response $\tilde{g}_{\mathrm{TRX}}(t)$ defined in (54) to build it.

Finally, from (56) and (57) we write the expression for the equalizer coefficients and the post-equalization noise variance:

$$\widetilde{\mathbf{w}} = \tilde{R}_{x\mathbf{Y}} \cdot \tilde{R}_{\mathbf{YY}}^{-1} \tag{60}$$

$$\sigma^2_{\mathrm{MMSEE,FLE}} = \bar{\mathcal{E}}_{\mathbf{x}} - \widetilde{\mathbf{w}} \cdot \tilde{R}_{\mathbf{YY}} \cdot \widetilde{\mathbf{w}}^{\dagger} \tag{61}$$

Then the unbiased SNR for FLE without noise whitening is obtained as follows.

$$\mathrm{SNR}_{\mathrm{MMSEE,FLE}} = \frac{\bar{\mathcal{E}}_x}{\sigma^2_{\mathrm{MMSEE,FLE}}} - 1 \tag{62}$$

The numerical conditioning of the finite-length models is governed by the covariance matrix used to compute the MMSE equalizer coefficients. In the WFLE, the whitening operation requires $S_{\mathrm{tot}}(f) > 0$; if the colored-noise PSD has zeros or very deep notches, $1/\sqrt{S_{\mathrm{tot}}(f)}$ may become ill-conditioned and may generate long temporal tails in the equivalent pulse response $h(t)$. The non-whitened FLE avoids this explicit whitening step by directly assembling the sampled colored-noise covariance in $\widetilde{\mathbf{R}}_{\mathbf{YY}}$. Tight filtering or nearly singular spectra may still increase the condition number of the covariance matrices, although no numerical instability was observed for the filtering conditions considered in this work and no additional regularization was required. In the reported implementation, the equalizer coefficients are computed through explicit matrix inversion, which was stable in all considered cases. For more severe configurations, a safer implementation could solve the corresponding linear system without explicitly forming the inverse and, if needed, use diagonal loading, namely $\widetilde{\mathbf{R}}_{YY} + \lambda\mathbf{I}$, after verifying that the selected λ has negligible impact on the predicted Q^2_{dB}.

TABLE 4. Fitting parameters for characterizing the optical filters based on the experimental power spectrum of Figure 9. B_{ch}: channel bandwidth; BW_{OTF}: optical-transfer-function bandwidth; DMX: demultiplexer; MUX: multiplexer.

	Nominal 50 GHz		Nominal 75 GHz	
Device	B_{ch}	BW_{OTF}	B_{ch}	BW_{OTF}
DMX 1	50.8 GHz	10.2 GHz	75.8 GHz	10.4 GHz
MUX 1	50.7 GHz	10.6 GHz	76.1 GHz	10.7 GHz
DMX 2	50.8 GHz	10.3 GHz	75.8 GHz	10.4 GHz
MUX 2	50.9 GHz	9.9 GHz	76.1 GHz	9.8 GHz

III. MODEL VALIDATION

This section is devoted to the validation of the mathematical models described in Section II. First we provide the mathematical model of the filtering devices, which has been exploited throughout the entire validation process. Then we show the results of the validation performed comparing the models with time-domain simulations, and finally the experimental results obtained replicating a realistic complex optical system with cascaded elements. Considerations are included, comparing the performance of the considered equalization algorithms and discussing the different effects on filtering penalty due to the interplay of ASE noise, transceiver impairment, and bandwidth limitation.

A. OPTICAL FILTER MODEL

The proposed models are general and can embed any scalar amplitude response of the optical filters. For validation purposes, the spectral response of the optical filters was modeled following the approach in [43], as was done in [10]. Such an optical filter model is well-suited to accurately represent the shape of the filtering effect when commercial ROADMs are deployed in the optical link, and is generally preferable to the super-Gaussian filter model. We emphasize that the adopted filter model neglects phase and polarization effects, since it provides only the amplitude effect of the optical filters.

The model assumes that the power spectrum of the WSS, which operates as a bandpass optical filter, is obtained by an aperture formed at the image plane of spatially diffracted light. In the frequency domain, the aperture width is related to the bandwidth B_{ch}. The output amplitude spectrum is then the convolution of the aperture function and the optical transfer function of the device [43], leading to the expression:

$$S(f) = \frac{1}{2}\sigma\sqrt{2\pi}\left[\mathrm{erf}\left(\frac{\frac{B_{\mathrm{ch}}}{2} - f}{\sigma\sqrt{2}}\right) - \mathrm{erf}\left(\frac{-\frac{B_{\mathrm{ch}}}{2} - f}{\sigma\sqrt{2}}\right)\right] \tag{63}$$

where $\sigma = BW_{\mathrm{OTF}}/(2\sqrt{2\ln 2})$ depends on the bandwidth of the optical transfer function BW_{OTF} of the WSS.

In the case of simulations, the parameter BW_{OTF} was set to 11 GHz, while B_{ch} was varied to test different filtering configurations. In the case of experiments, the optical spectrum analyzer (OSA) traces of the filter spectra were fitted by adjusting both the B_{ch} and the BW_{OTF} parameters. The fitting parameters are provided in Table 4, while the fitted power spectra are reported in Figure 9. Equation (63) accurately models the shapes of the four filters at the two

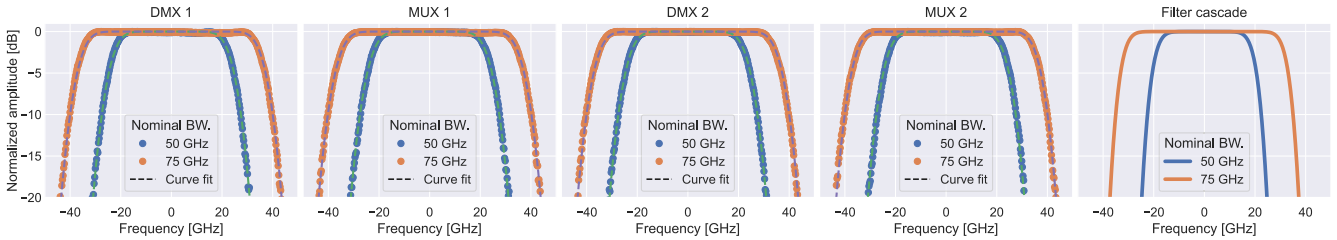

FIGURE 9. Experimental characterization of the optical filters.

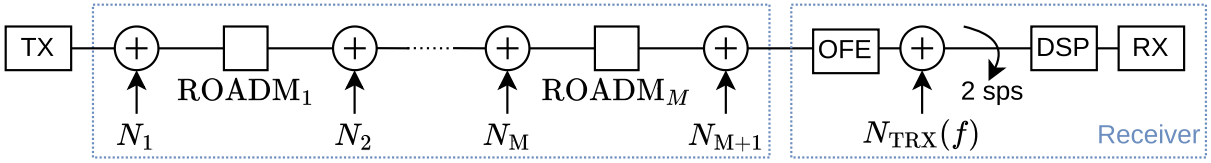

FIGURE 10. Reference setup for time-domain simulation with $M = 10$ filtering stages.

tested bandwidths and can therefore be used in the filtering model. The same Figure 9 also reports the shape of the cascade of the filters, which helps visualize how the overall bandwidth shrinks when four filters are placed one after the other.

B. SIMULATIONS

We performed the model validation through time-domain simulations, exploiting the software validated in [11]. The adopted simulator implements a least-mean-squares (LMS) algorithm to estimate the received symbol sequence, allowing the desired number of equalizer taps to be set. We compared the post-equalization SNR provided by the simulator with the values computed using all the models described in section II.

For validation purposes, we selected an arbitrary network setup containing ten identical filtering elements, replicating the filtering effect experienced by the signal when crossing ROADMs in network nodes. As anticipated, we adopted the optical filter model proposed in [43], according to the filter shape of (63) setting the parameter $BW_{\text{OTF}} = 11$ GHz and tuning the parameter B_{ch} to obtain the desired equivalent 3-dB bandwidth of the filter cascade. We emphasize that the simulation allowed us to test the developed models on a scale unachievable in a laboratory environment, both in terms of number of elements and extreme filtering configurations. To make meaningful comparisons of noise-location effects, the noise sources can be placed before, after, or interspersed throughout the filter chain. Figure 10 visually details the scenario, in which the different noise sources can be enabled or disabled as needed, and the transmitted signal is shaped by a root-raised-cosine (RRC) pulse at a symbol rate of 64 GBd, DP-QPSK modulation, and roll-off equal to 0.15. Noise sources are tuned so that their combined effect produces an SNR_{ASE} of 12 dB, while the receiver is always characterized by a 20 dBSNR_{TRX}, with a white PSD. This choice was made to prevent the filtering penalty from being dominated by transceiver noise. In fact, if transceiver noise is the main impairment, a different displacement of ASE noise along the optical link does not lead to significantly different performance.

For mathematical models and simulation results, performance is assessed by evaluating the Q^2_{dB} factor, as defined in (2). The BER used in Q-factor evaluation is derived from the standard BER formula for DP-QPSK modulation:

$$\text{BER} = \frac{1}{2}\text{erfc}\left(\sqrt{\frac{\text{SNR}_{\text{EQ}}}{2}}\right) \tag{64}$$

where SNR_{EQ} is the post-equalization SNR, and is computed from (28), (33), (35), (46), and (62) for theoretical models; otherwise, it is provided directly by the time-domain simulator.

1) MODEL VALIDATION VERSUS THE NUMBER OF TAPS

The first validation step compared the different equalizer models with the results provided by the time-domain simulator, varying the number of taps used in the LMS algorithm and the total equivalent 3-dB bandwidth of the filtering cascade. ASE noise was uniformly distributed among the noise sources. The maximum absolute errors for all the equalization models and simulation configurations are summarized in Table 5.

Figure 11 illustrates that an increase in the number of taps of the LMS algorithm allows an improvement in the estimation of the received signals, which in turn increases the Q^2_{dB} factor. In particular, with 4 or 8 taps there is a non-negligible gap between finite and infinite equalizer models, since MMSEE and FSE cannot predict the limited-tap penalty. In contrast, increasing the LMS taps to 64 makes all the results converge. Additionally, MMSEE and FSE always provide the same result, as expected, since they are both based on mean-square error. Indeed, in practical applications using commercial transceivers, an FSE employing algorithms such as least-mean-squares or constant-modulus adaptation converges to MMSEE performance [42].

TABLE 5. Summary of the filtering penalty estimation absolute errors and RMSE for validation by means of time-domain simulation for different numbers of taps of the LMS equalizer. In the second group of columns, we considered only the cases in which the bandwidth of the cascade of the optical filters was larger than 90% of the symbol rate.

	Max. Abs. Error on Q^2_{dB} [dB]				Max. Abs. Error on Q^2_{dB} [dB] when $B_{3dB} > 90\%$ of R_s				RMSE [dB]			
Models \ Taps	4	8	16	64	4	8	16	64	4	8	16	64
ZFE	-	-	-	-	1.24	0.81	0.39	0.87	-	-	-	-
MMSEE	1.56	1.15	0.69	0.21	1.56	1.15	0.69	0.18	0.92	0.65	0.37	0.12
FSE	1.56	1.15	0.69	0.21	1.56	1.15	0.69	0.18	0.92	0.65	0.37	0.12
WFLE	0.41	0.25	0.20	0.15	0.41	0.24	0.19	0.12	0.22	0.16	0.12	0.09
FLE	0.29	0.20	0.17	0.15	0.29	0.19	0.15	0.12	0.16	0.11	0.10	0.09

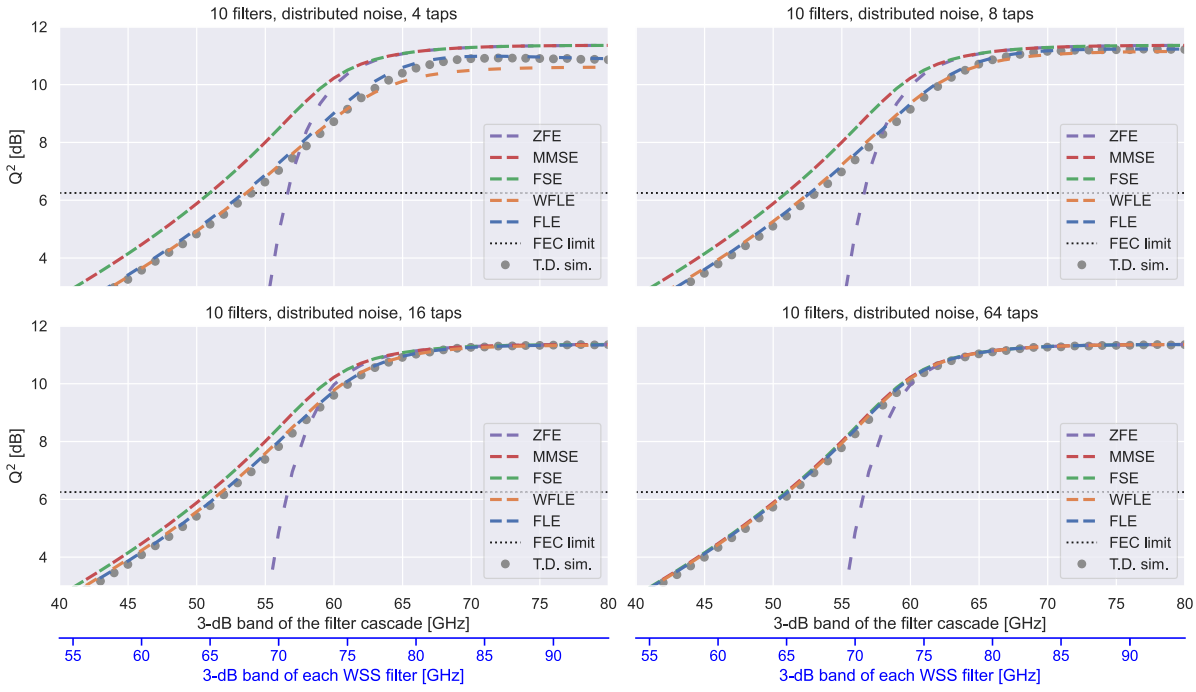

FIGURE 11. Equalizer model comparison and validation with time-domain simulations.

Regarding the WFLE and the FLE, we observe that, with 4 taps, there is a small difference between the two models. In particular, the WFLE is conservative with respect to time-domain simulation, with a maximum error of 0.41 dB, while the FLE follows the time-domain simulation results extremely accurately, with a maximum error of 0.29 dB. Nevertheless, when the number of taps increases, as depicted for 8, 16 and 64 taps in Figure 11, the WFLE almost overlaps the FLE, with a difference in the estimation error lower than 0.05 dB. One explanation to consider is that as the number of taps increases, the scenario approaches the infinite-length-equalizer case, in which the presence of the whitening filter is no longer an approximation. Notably, the WFLE also provides very reliable predictions with 8 and 16 taps, with a maximum absolute error of 0.25 dB and 0.20 dB, where there is a non-negligible gap between the predictions of finite- and infinite-length equalizer models. Therefore, in addition to the number of taps, it is also necessary to consider the total amount of noise and the way in which the channel pulse response is truncated. All these parameters affect the dimensions and values of the channel matrices introduced in Section II-F. FLE significantly outperforms MMSEE and FSE for all the considered values of the number of taps. FLE is also more accurate than the WFLE, but in this case the difference between the two models becomes significant only with 4 taps.

These results explain why the WFLE approach has been successfully adopted in previous works, even for finite-length equalization [27], but in general the FLE should be preferred, being more realistic and giving the best prediction performance, as summarized in Table 5, where we also provide the RMSE, computed considering all the points for each model-taps combination.

Lastly, the ZFE gives the worst performance prediction, when the equivalent bandwidth of the filter cascade is significantly lower than the signal symbol rate, due to strong noise enhancement when the filters are tight. Nevertheless, when the number of taps of the LMS algorithm is equal to

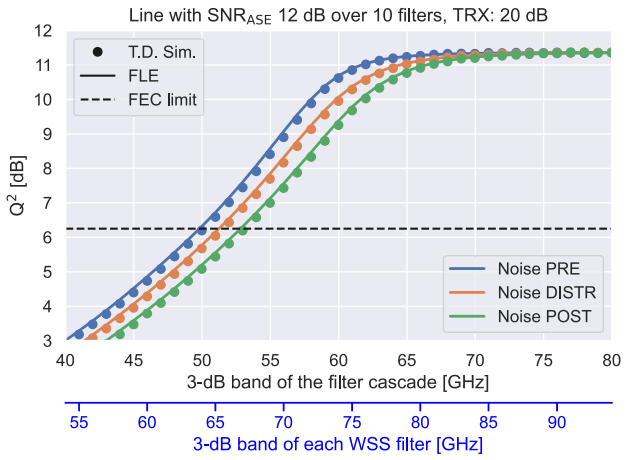

FIGURE 12. Comparison of the Q^2_{dB} evolution with different filter cascade bandwidths and noise positions. FLE equalizer with 32 taps.

64, even the very light and simple ZFE gives a conservative and good assessment of the filtering penalty down to an equivalent filter cascade bandwidth of approximately 90% of the symbol rate, with a maximum absolute error of 0.87 dB. This observation is important because in a realistic scenario the overall filtering effect is not expected to be extreme, and commercial transceivers have a number of taps on the order of a few tens. Therefore, even the ZFE could be a good choice as a mathematical model, allowing fast penalty estimation and disaggregation, as anticipated in Section II-E.1. This result is pivotal for the development of an ONDT.

2) MODEL VALIDATION VERSUS NOISE POSITION

In the second validation test, the number of LMS taps was set to 32, and the ASE noise was injected at different locations: entirely at the first source in the pre-filter (PRE) configuration, entirely at the last source in the post-filter (POST) configuration, and uniformly across sources in the distributed (DISTR) configuration. In this way, we explored how the interplay of filtering effect and noise distribution affects the system performance. In all three cases $\mathrm{SNR}_{\mathrm{ASE}}$ was kept constant and equal to 12 dB, as in the previous validation test, and $\mathrm{SNR}_{\mathrm{TRX}}$ was again set to 20 dB.

The time-domain simulation results were compared with the FLE mathematical model, as reported in Figure 12. In this second test, very close agreement is also observed between the mathematical model and the points simulated using the LMS algorithm, with a maximum absolute error of 0.17 dB for PRE, 0.15 dB for DISTR, and 0.14 dB for POST. Performance also depends on the relative position of noise and filtering elements. When noise is injected after the filter cascade, the SNR penalty is higher because equalization restores the signal while more strongly enhancing receiver-side noise. Conversely, noise injected closer to the transmitter passes through the full filter cascade, reducing equalizer-induced enhancement. Since receiver-side noise experiences the strongest filtering penalty, NLI can be conservatively modeled as AWGN injected at the receiver, as anticipated in Section I-A. As shown in Figure 12, for the considered optical link, the minimum filter-cascade 3-dB bandwidth differs by about 4 GHz at the forward error correction (FEC) BER limit of 2×10^{-2}.

3) COMPUTATIONAL COMPLEXITY ANALYSIS

The computational complexity must be carefully considered in order to evaluate the suitability for ONDT implementations. Despite being much faster than time-domain simulation, the matrix-based FLE is the most computationally demanding among the considered equalization models. Based on the FLE model described in Section II-F.2, a naive dense-matrix implementation requires the construction of the signal covariance contribution, the assembly of the colored-noise covariance contributions, and the solution of the MMSE linear system. The corresponding computational cost is$O\left((N_f\ell)^2(N_f+\nu)+(M+2)(N_f\ell)^2((N_f+\nu+1)\ell-1)+(N_f\ell)^3\right)$ The first term is associated with the computation of $\widetilde{\mathbf{H}}\widetilde{\mathbf{H}}^{\dagger}$, the second one with the $M+2$ colored-noise covariance contributions $\widetilde{\mathbf{G}}_i\widetilde{\mathbf{G}}_i^{\dagger}$ and $\widetilde{\mathbf{G}}_{\mathrm{TRX}}\widetilde{\mathbf{G}}_{\mathrm{TRX}}^{\dagger}$, and the third one with the solution of the linear system involving $\widetilde{R}_{\mathbf{YY}}$. Therefore, the dependence on M arises from the covariance-assembly stage, whereas the dense linear-system solution scales as $O((N_f\ell)^3)$ for fixed N_f, ℓ, and ν. If ℓ and ν are fixed by the receiver sampling rate and by the selected impulse-response truncation accuracy, respectively, the dominant FLE cost can be compactly summarized as $O(M(N_f\ell)^3)$. This compact notation should be interpreted as the asymptotic scaling of the overall dense implementation, not as an indication that the matrix inversion itself is repeated for each noise source. For the WFLE, the whitening assumption avoids the explicit assembly of the colored-noise covariance matrices for all noise sources. The corresponding dense implementation has complexity $O\left((N_f\ell)^2(N_f+\nu)+(N_f\ell)^3\right)$, which can be compactly written as $O((N_f\ell)^3)$ under the same assumptions. The ZFE, MMSEE, and FSE models require only numerical integration over the frequency grid and do not involve finite-length covariance matrices. Their cost is independent of N_f and ν, and is negligible with respect to the finite-length models for the grid sizes considered in this work.

C. EXPERIMENTS

Model validation was performed experimentally using the setup depicted in Figure 13, which incorporates four WSSs (two multiplexers (MUXs) and two demultiplexers (DMXs)) acting as optical filters. An optical signal was transmitted by the two commercial transceivers characterized in Section I-B, referred to as Vendor A and Vendor B. In the case of Vendor A, the device was a pluggable transceiver with a simpler architecture than the Vendor B transceiver. The transceivers allowed measurement of the ROP and the BER of the received signal. BER results were converted in terms of Q^2_{dB} factor, as anticipated in Section I-A, according to (2). For both transceivers, the central frequency was 193.5 THz, and the transmitted signal was shaped with an RRC pulse whose

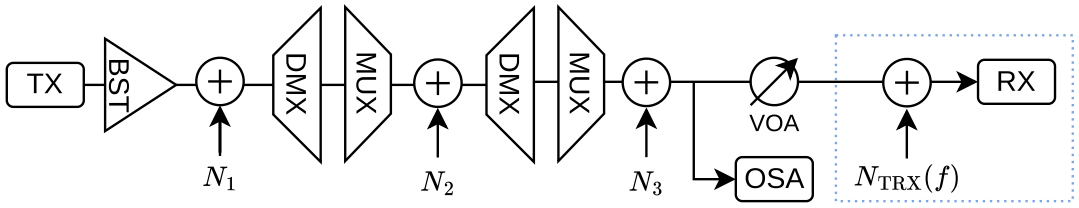

FIGURE 13. Experimental setup. BST: booster amplifier; OSA: optical spectrum analyzer; VOA: variable optical attenuator.

symbol rate is reported in Table 1, with roll-off factors of 0.2 for Vendor A and 0.1 for Vendor B.

To guarantee the necessary power budget, an additional booster amplifier was incorporated at the beginning of the optical link, mitigating the intrinsic loss introduced by the WSSs. A VOA was used to tune the ROP and, consequently, the impact of the transceiver noise through the parameter $\mathrm{SNR}_{\mathrm{TRX}}$.

For the experiments, the WSSs were centered around 193.5 THz, as for the transmitted signal. According to Table 1, when the symbol rate was 31.6 GBd or 34.7 GBd, the optical filter bandwidth was set to 50 GHz; in the other cases, the selected optical filter bandwidth was 75 GHz. The filter shapes are those described in Section III-A and reported in Figure 9.

The three ASE noise sources were characterized using an OSA and adjusted to ensure that they all provided the same impact on the signal quality, so that the ASE noise impairment was uniformly distributed along the optical link. It was possible to tune the ASE sources to set the desired total $\mathrm{SNR}_{\mathrm{ASE}}$.

The bandwidth of the WSSs could be adjusted in steps of 12.5 GHz, which did not allow us to test many filtering conditions. To achieve a tight and asymmetric filtering condition, we shifted the central frequency of the transceiver rather than acting on the parameters of the optical filters. This controlled misalignment resulted in a progressive distortion of the spectral shape of the signal and a gradual increase in the associated penalty. The same shifts were also applied to the transmitted signal in the mathematical model. As will be detailed in the following, the two considered transceivers provided different levels of control over the central-frequency shift; therefore, for Vendor B it was possible to collect more curves.

For both Vendor A and Vendor B, the parameter $\mathrm{SNR}_{\mathrm{TRX}}$ was independently characterized using (7), as described in Section I-B. For Vendor A the transceiver noise is modeled as an AWGN source at the end of the link, with ideal AA filtering and without any further bandwidth limitation in the electrical domain. In the case of Vendor B, it was possible to characterize the AA filter based on the ADC samples, but an additional effort was needed, considering a transceiver noise with colored PSD.

For both Vendor A and Vendor B transceivers, the experimental curves are compared with the outputs of the WFLE and FLE models. We chose them among the models discussed in Section II because they are the most realistic ones, based on mean-square-error estimation and with a finite number of transceiver taps. In this way, we further explore the differences between the two models in terms of accuracy.

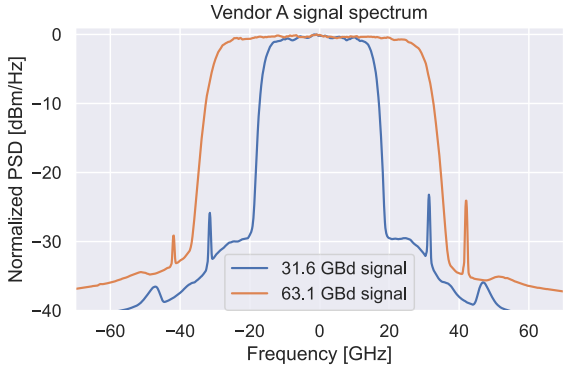

FIGURE 14. Spectrum of the signal transmitted by the Vendor A transceiver, measured with an OSA.

1) VENDOR A

In this first case, knowledge of the internal workings of the pluggable transceiver and control options was limited compared to the more sophisticated transceiver of Vendor B. Consequently, we limited the theoretical assumptions to the simpler ones, namely white transceiver noise and no additional filtering impairments in the electrical domain. This framework was consistent with all the modeling provided in Section II, and the experimental validation was successful. From the control point of view, the allowed central frequency shifts were limited and available only with coarse step sizes. We were able to test high filtering penalty configurations, but with a coarse granularity.

In Figure 14 the measurement of the spectrum of the transmitted signal for Vendor A is reported. The spectral "horns" visible at the band edges are attributed to auxiliary spectral components introduced by the transceiver implementation, typically associated with timing and synchronization functions within the DSP chain. Although they do not carry payload information, they contribute to maintaining receiver synchronization and enabling performance monitoring. When optical filtering strongly attenuates these edge components, the receiver may lose the ability to correctly recover timing or estimate performance metrics such as BER, leading to operational failure even if the central portion of the signal spectrum remains detectable. As a consequence, the maximum range of filtering configurations that could be experimentally investigated was limited. This limitation does not make the Vendor

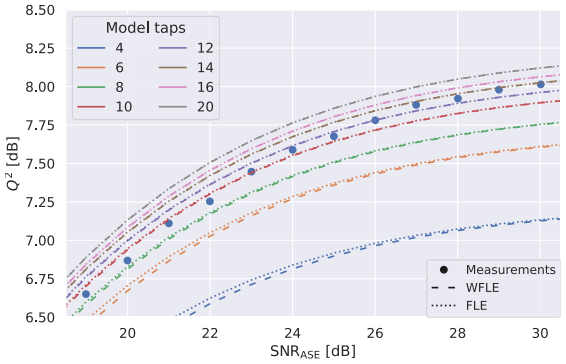

FIGURE 15. Comparison of equalization models and measurements for different numbers of taps for Vendor A, considering DP-16QAM 400G modulation with ROP equal to -22.5 dBm and centered optical filters.

TABLE 6. Estimated RMSE between models and measurements for different numbers of taps for Vendor A, considering DP-16QAM 400G modulation with ROP equal to -22.5 dBm.

Taps	WFLE [dB]	FLE [dB]
4	0.7796	0.7572
6	0.3283	0.3156
8	0.1898	0.1852
10	0.0789	0.0795
12	**0.0692**	**0.0718**
14	0.1041	0.1056
16	0.1338	0.1351
20	0.1823	0.1830

A validation secondary, since the accessible configurations still include centered cascaded filtering through four WSSs and, in most cases, asymmetric filtering with frequency shifts equal to 6 or 7 GHz. These measurements therefore validate the model within the operating region in which the pluggable transceiver remains synchronized and provides reliable BER estimates, while no claim is made for operational-failure regimes.

First, we estimated the number of taps of the equalizer. We chose DP-16QAM 400G modulation, which is the most interesting from a commercial point of view, at an ROP of -22.5 dBm. We compared WFLE and FLE with the case of centered optical filters, computing the RMSE for different numbers of taps. This case, which was used to calibrate the model, was not considered in computing the errors on blind test data, and the same approach was used in the case of Vendor B. The calibration process is summarized in Table 6, and Figure 15 gives a qualitative visualization of it. For both WFLE and FLE, the estimated number of taps was 12, which is reasonable considering the specifics of the pluggable transceiver under test. The corresponding maximum absolute error was 0.29 dB.

Figure 16 reports the measured Q^2_{dB} factor as a function of SNR_{ASE} for different modulation formats, baud rates, and ROPs under several optical filtering configurations. For each modulation format, three ROP values have been tested: -17.5 dBm, -20 dBm, and -22.5 dBm. The first measurement run, corresponding to the blue dotted curves in Figure 16, was carried out without a significant filtering penalty, setting the bandwidth of the optical filters to 200 GHz. Then symmetric filtering with filters and the transmitted signal centered on 193.5 THz was assessed and is shown by the orange dotted curves in Figure 16. After this second test, different shifts of the central frequency of the transceiver were tried, in order to validate the mathematical model with asymmetric filtering conditions. The limited control of the transceiver allowed us to test a shift close to 6 or 7 GHz for most of the cases. For this reason, for DP-16QAM 400G modulation we were not able to test any asymmetric filtering configuration, but only the case in which the transceiver central frequency was the same as that of the optical filters. The Vendor A results should therefore be interpreted as a validation over a restricted but still meaningful set of filtering conditions. In particular, the centered-filter case is not penalty-free, because the cascade of four WSSs already narrows and reshapes the signal spectrum, while the available 6/7 GHz frequency shifts provide additional asymmetric-filtering stress for the configurations in which the transceiver remained operational.

The penalty depends strongly on modulation format and symbol rate. DP-QPSK shows limited degradation, confirming its robustness to spectral shaping and bandwidth constraints. DP-16QAM has larger penalties, especially at higher baud rates such as 400G, due to greater sensitivity to filtering-induced ISI and constellation distortion. ROP also affects performance: lower power shifts the curves downward because transceiver noise increases under suboptimal operating conditions.

Within the experimentally accessible region, a generally good agreement is observed between the analytical models and experimental measurements, with an overall maximum absolute error of 0.36 dB. A detailed case-by-case error report is provided in the error analysis in Section III-C.3, separating calibration errors and errors on blind test data. For this transceiver, there are no significant differences between WFLE and FLE in terms of performance predictions, with the FLE being slightly more accurate in most of the cases.

In 16a and 16d, saturation occurs at high SNR_{ASE} levels and is not reproduced by the model curve, represented by empty bullets. As anticipated in Section I-B, this happens because at 15.5 dB of Q^2_{dB} level, for DP-QPSK modulation, the measured BER ranges between 10^{-10} and 10^{-9}, tending to saturate, being estimated only on the overhead bits. For this reason, saturated DP-QPSK points were not included in the error computation and in the error analysis.

2) VENDOR B

The transceiver under test in this second part of the experimental validation was more sophisticated than the pluggable transceiver from Vendor A, allowing testing of more filtering configurations with finer granularity. In addition, in this case there were no clock-recovery or synchronization issues under severe filtering. This is confirmed by looking at the measured spectrum of the transmitted signal, provided in Figure 17,

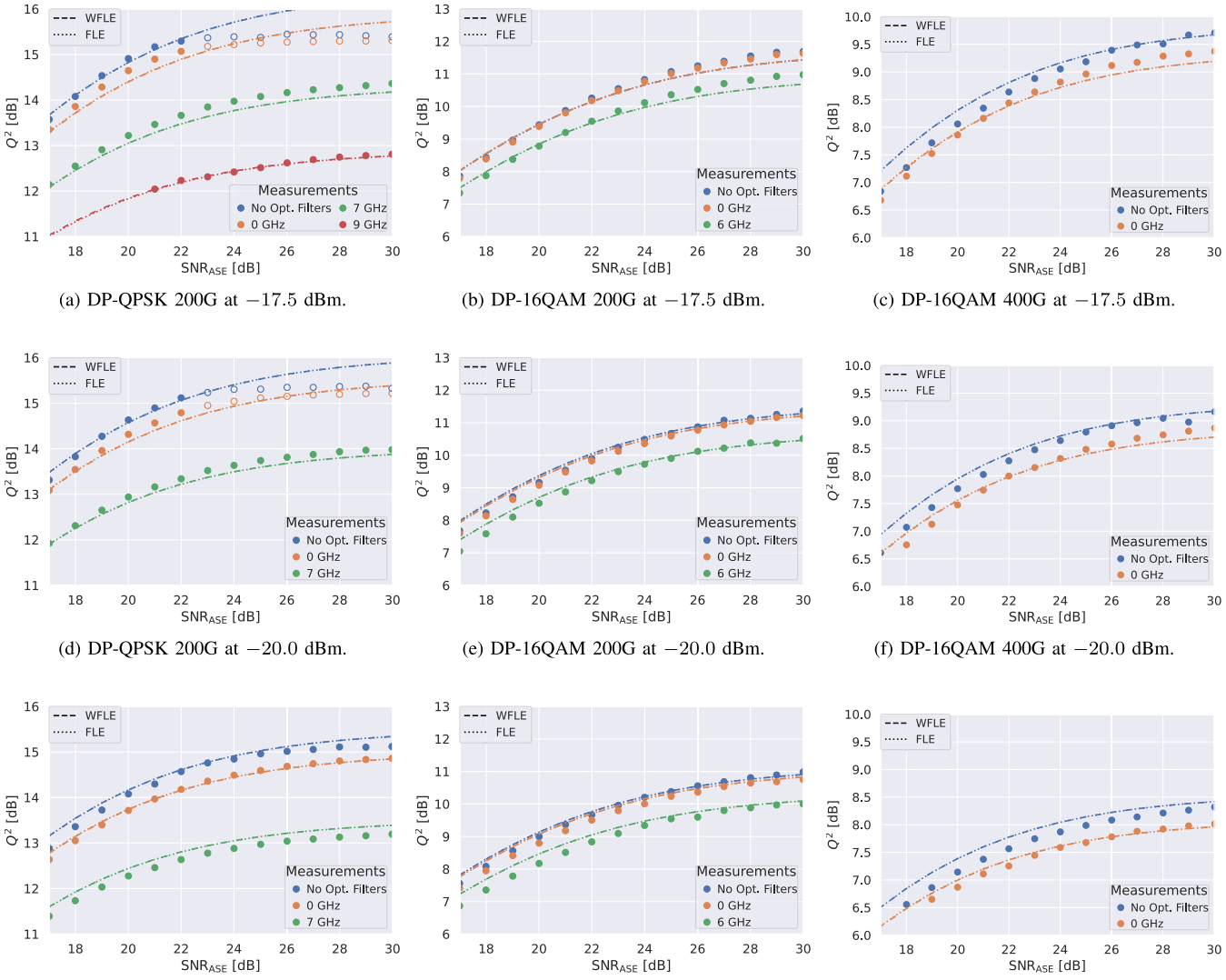

(a) DP-QPSK 200G at −17.5 dBm. (b) DP-16QAM 200G at −17.5 dBm. (c) DP-16QAM 400G at −17.5 dBm.

(d) DP-QPSK 200G at −20.0 dBm. (e) DP-16QAM 200G at −20.0 dBm. (f) DP-16QAM 400G at −20.0 dBm.

(g) DP-QPSK 200G at −22.5 dBm. (h) DP-16QAM 200G at −22.5 dBm. (i) DP-16QAM 400G at −22.5 dBm.

FIGURE 16. Vendor A transceiver: experimental results for different ROPs and modulation formats. Comparison with WFLE and FLE mathematical models assuming 12 taps. DP-16QAM 400G, ROP −22.5 dBm, and a frequency shift of 0 GHz were used for calibration; the other curves are part of the blind validation.

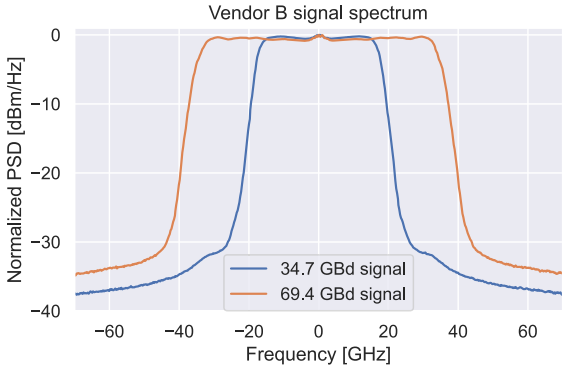

FIGURE 17. Spectrum of the signal transmitted by the Vendor B transceiver, measured with an OSA.

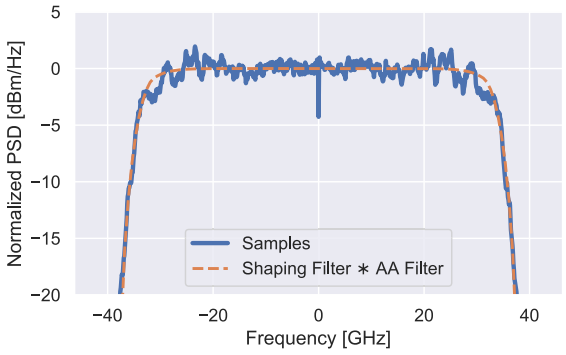

FIGURE 18. Vendor B transceiver: estimated PSD of ADC samples and AA filter tuning. The AA filter was estimated to be a sixth-order super-Gaussian filter with a bandwidth of 69.4 GHz.

where no edge spectral components are visible or required to maintain transceiver synchronization.

Moreover, post-ADC samples were accessible, from which we estimated the transfer function of the AA filter. Figure 18

shows the PSD of the ADC samples estimated using Welch's method [44], together with the fit obtained by multiplying the transmitted RRC spectrum of Figure 17 by a sixth-order super-Gaussian filter with a bandwidth of 69.4 GHz. As a consequence, in this second case we had to account for the electrical bandwidth limitation, which was considered as an additional filtering stage after the injection of transceiver noise according to Figure 3. The presence of the AA filter does not require any modification to the models developed in Section II, but it causes significant differences between WFLE and FLE models. We recall that the FLE matrix construction includes the AA filter shape, while in the case of WFLE the transfer function of the AA filter cancels out, leading to approximations.

In addition to the electrical bandwidth limitation, for this second transceiver, the basic hypothesis of white transceiver noise is not sufficient to obtain consistent results. Indeed, it is possible to fit the back-to-back curves, as was done to characterize the transceiver in Figure 4, exploiting the term $\mathrm{SNR}_{\mathrm{TRX}}$ to obtain the equivalent white noise and tuning the mathematical model to match the experimental results in the absence of optical filtering. Nevertheless, this process is insufficient because the model is inconsistent with the measurements when optical filtering is applied. The amount of ASE noise is experimentally controlled, and the optical and electrical filtering effects are characterized in detail and independently of $\mathrm{SNR}_{\mathrm{TRX}}$. Therefore, the noise introduced by the transceiver must have a colored PSD. We propose a heuristic method tailored to commercial transceivers and application-oriented scenarios.

Owing to the bandwidth limitation introduced by the AA filter, equalization corrects the received signal even in the back-to-back configuration. Therefore, the fitted $\mathrm{SNR}_{\mathrm{TRX}}$ cannot be directly interpreted as the ratio between the ROP and an AWGN transceiver-noise power, as in (15). In principle, the shape $S_{\mathrm{TRX}}(f)$, the factor $\dot{N}_{\mathrm{TRX}}$, and the number of equalizer taps should be estimated using the FLE model within an optimization loop. However, for back-to-back measurements, the impact of the finite equalizer length is limited; hence, an infinite-length model provides a reliable approximation, consistently with the observations in [20]. Accordingly, we use the MMSEE model to iteratively optimize $\dot{N}_{\mathrm{TRX}}$ and $S_{\mathrm{TRX}}(f)$ by matching the following estimate $\widetilde{\mathrm{SNR}}_{\mathrm{TRX}}$ to the experimentally measured $\mathrm{SNR}_{\mathrm{TRX}}$:

$$\widetilde{\mathrm{SNR}}_{\mathrm{TRX}} = \frac{\mathrm{ROP}}{\dot{N}_{\mathrm{TRX}} \displaystyle\int_{-\frac{R_s}{2}}^{\frac{R_s}{2}} \frac{df}{Q\left(e^{-j\frac{2\pi f}{R_s}}\right) + \frac{\dot{N}_{\mathrm{TRX}} R_s}{\mathrm{ROP}}}} - 1 \tag{65}$$

where

$$Q\left(e^{-j\frac{2\pi f}{R_s}}\right) = \frac{\left|\Phi\left(e^{-j\frac{2\pi f}{R_s}}\right)\right|^2}{S_{\mathrm{TRX}}\left(e^{-j\frac{2\pi f}{R_s}}\right)} \tag{66}$$

In Figure 19, we plot the shape of the PSD $S_{\mathrm{TRX}}(f)$ as seen after the AA filter. The accuracy of the proposed heuristic method can be further improved when the ground-truth PSD of the transceiver noise is available, since its shape is strongly device-dependent and may exhibit complex and diverse spectral profiles [45]. In the present study, this information was not available because the internal operation of the Vendor B transceiver was not accessible.

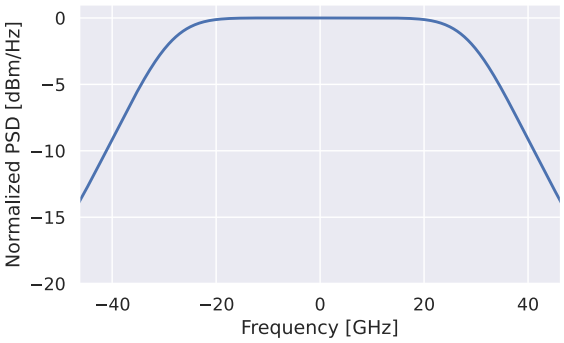

FIGURE 19. Vendor B transceiver: heuristic model of the colored PSD after the AA filter.

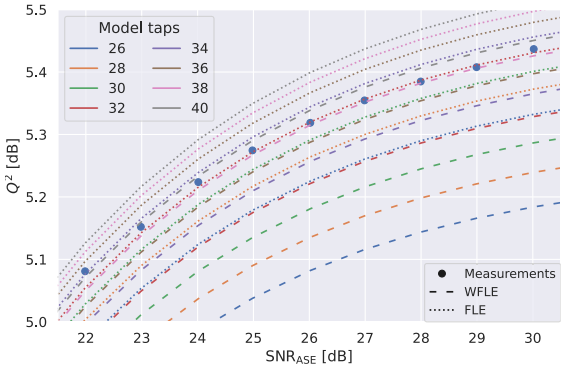

FIGURE 20. Comparison of equalization models and measurements for different numbers of taps for Vendor B, considering DP-16QAM 400G modulation with ROP equal to -22.5 dBm. Central frequencies of optical filters were shifted by 5 GHz.

TABLE 7. Estimated RMSE between models and measurements for different numbers of taps for Vendor B, considering DP-16QAM 400G modulation with ROP equal to -22.5 dBm. Central frequencies of the optical filters were shifted by 5 GHz.

Taps	WFLE [dB]	FLE [dB]
26	0.2430	0.1006
28	0.1900	0.0622
30	0.1446	0.0355
32	0.1045	**0.0108**
34	0.0694	0.0207
36	0.0392	0.0419
38	**0.0142**	0.0584
40	0.0159	0.0736

After selecting the spectral shape $S_{\mathrm{TRX}}(f)$ and the scaling factor $\dot{N}_{\mathrm{TRX}}$, we estimated the number of taps by selecting the case with ROP equal to -22.5 dBm and DP-16QAM 400G modulation, and computing the RMSE between the measurements and the WFLE and FLE models. We chose the case where optical filters were shifted by 5 GHz (the maximum shift available), in which the effect of the limited number of taps is expected to be more significant. This case

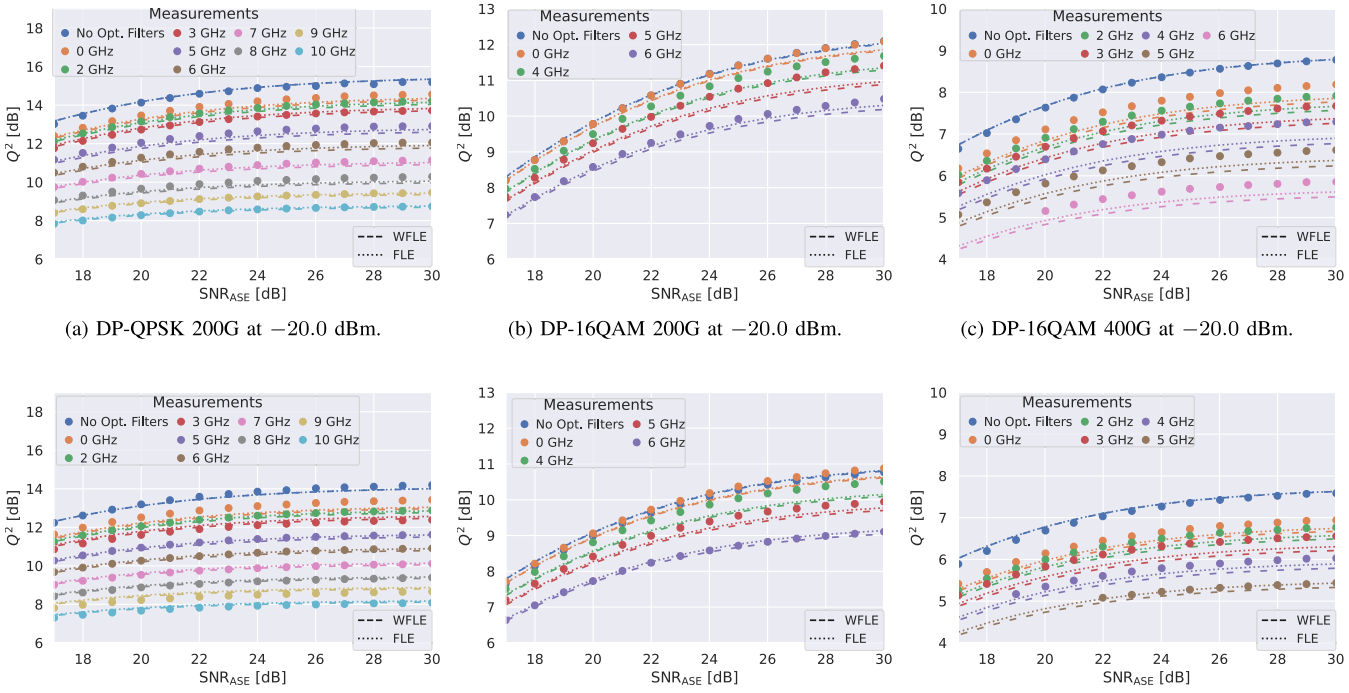

(a) DP-QPSK 200G at −20.0 dBm. (b) DP-16QAM 200G at −20.0 dBm. (c) DP-16QAM 400G at −20.0 dBm.

(d) DP-QPSK 200G at −22.5 dBm. (e) DP-16QAM 200G at −22.5 dBm. (f) DP-16QAM 400G at −22.5 dBm.

FIGURE 21. Vendor B transceiver: experimental results for different ROPs and modulation formats. Comparison with WFLE and FLE mathematical models assuming 32 taps. DP-16QAM 400G, ROP −22.5 dBm, and a frequency shift of 5 GHz were used for calibration; the other curves are part of the blind validation.

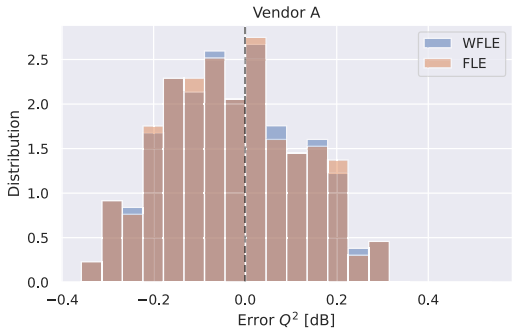

FIGURE 22. Experimental prediction error distribution in the case of Vendor A on blind test data. Calibration errors and errors for saturated DP-QPSK points were not considered.

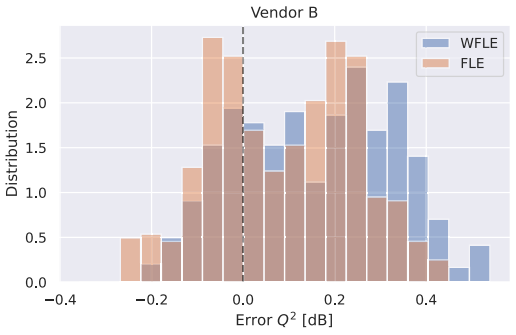

FIGURE 23. Experimental prediction error distribution in the case of Vendor B on blind test data. Calibration errors were not considered.

was used for model calibration and was not used to compute the prediction errors on blind test data. We report the results in Table 7. Based on the FLE results, which correspond to the most realistic model we have, we estimate that the number of taps is 32. Figure 20 visualizes the estimation process. We observe that for Vendor B there are significant differences between the WFLE and FLE, confirming the conservativeness of WFLE. This comment will be quantitatively expanded in what follows.

Figure 21 provides a detailed visual validation of the FLE analytical model by comparing the predicted Q^2_{dB} values, shown as dashed and dotted curves, with experimental measurements, shown as markers. The comparison is performed under controlled frequency offsets between the signal and the central frequency of the optical filter cascade, for different modulation formats and ROP values. The model reproduces the measurements with good accuracy across all the investigated modulation formats and ROPs, with maximum absolute errors of 0.53 dB for the WFLE and 0.42 dB for the FLE. The FLE consistently outperforms the WFLE in all the explored cases, reducing the absolute error by approximately 0.1 dB on average. The prediction errors on blind test data are reported in the error analysis in Section III-C.3 for all the considered combinations of modulation formats, ROPs, and optical-filtering severity. These results confirm that modeling the transceiver noise as colored, rather than white, is essential. Indeed, equalization reshapes the noise spectrum, and the resulting noise enhancement depends on the overlap between the equalizer transfer function and the non-flat noise PSD, an effect that cannot be captured by a white-noise approximation.

TABLE 8. Experimental errors versus filtering severity, modulation format, and ROP in the case of Vendor A, considering WFLE with 12 taps. Calibration errors are shown in blue. The maximum absolute prediction error is shown in red.

Metric	Modulation	ROP [dBm]	Optical-filter central-frequency shift [GHz]				
			No filter	0	6	7	9
Maximum Absolute Error [dB]	DP-QPSK 200G	-17.5	0.10	0.25	-	0.21	0.04
		-20.0	0.17	0.18	-	0.15	-
		-22.5	0.28	0.14	-	0.21	-
	DP-16QAM 200G	-17.5	0.31	0.24	0.31	-	-
		-20.0	0.27	0.30	0.30	-	-
		-22.5	0.22	0.30	0.33	-	-
	DP-16QAM 400G	-17.5	**0.36**	0.19	-	-	-
		-20.0	0.26	0.21	-	-	-
		-22.5	0.29	**0.13**	-	-	-
RMSE [dB]	DP-QPSK 200G	-17.5	0.07	0.19	-	0.17	0.03
		-20.0	0.08	0.13	-	0.12	-
		-22.5	0.15	0.06	-	0.18	-
	DP-16QAM 200G	-17.5	0.19	0.15	0.19	-	-
		-20.0	0.14	0.16	0.13	-	-
		-22.5	0.10	0.18	0.20	-	-
	DP-16QAM 400G	-17.5	0.18	0.12	-	-	-
		-20.0	0.14	0.11	-	-	-
		-22.5	0.20	**0.07**	-	-	-

TABLE 9. Experimental errors versus filtering severity, modulation format, and ROP in the case of Vendor B, considering WFLE with 32 taps. Calibration errors are shown in blue. The maximum absolute prediction error is shown in red.

Metric	Modulation	ROP [dBm]	Optical-filter central-frequency shift [GHz]										
			No filter	0	2	3	4	5	6	7	8	9	10
Maximum Absolute Error [dB]	DP-QPSK 200G	-20.0	0.17	0.33	0.19	0.08	-	0.35	0.31	0.23	0.31	0.10	0.05
		-22.5	0.19	0.45	0.12	0.16	-	0.13	0.11	0.04	0.06	0.20	0.12
	DP-16QAM 200G	-20.0	0.08	0.25	-	-	0.39	0.50	0.26	-	-	-	-
		-22.5	0.12	0.26	-	-	0.41	0.26	0.06	-	-	-	-
	DP-16QAM 400G	-20.0	0.09	0.41	0.36	0.43	**0.54**	0.38	0.37	-	-	-	-
		-22.5	0.14	0.28	0.28	0.35	0.25	**0.12**	-	-	-	-	-
RMSE [dB]	DP-QPSK 200G	-20.0	0.10	0.28	0.15	0.04	-	0.31	0.26	0.18	0.26	0.06	0.03
		-22.5	0.14	0.39	0.09	0.10	-	0.11	0.08	0.03	0.03	0.18	0.08
	DP-16QAM 200G	-20.0	0.05	0.18	-	-	0.30	0.37	0.19	-	-	-	-
		-22.5	0.07	0.20	-	-	0.34	0.23	0.04	-	-	-	-
	DP-16QAM 400G	-20.0	0.04	0.36	0.32	0.38	0.50	0.35	0.35	-	-	-	-
		-22.5	0.08	0.24	0.25	0.33	0.23	**0.10**	-	-	-	-	-

From a system perspective, the results show the combined impact of filtering, ASE noise, transceiver noise, equalizer limitations, and modulation sensitivity. At low $\mathrm{SNR}_{\mathrm{ASE}}$, additive noise dominates, so filtering asymmetry has a limited effect. As $\mathrm{SNR}_{\mathrm{ASE}}$ increases, asymmetric-filtering distortion becomes dominant, requiring a tradeoff between residual ISI suppression and noise amplification. This leads to larger separation among offset conditions and saturation of achievable Q^2_{dB}. The effect is stronger for DP-16QAM and higher symbol rates due to greater sensitivity to residual amplitude/phase errors and reduced equalization margin from tighter spectral occupancy. The ROP dependence follows the same considerations as for Vendor A, further highlighting the interplay between ASE and transceiver noise. Overall, the agreement confirms that incorporating colored transceiver noise and finite equalizer length is essential to accurately predict filtering penalties for the Vendor B transceiver, supporting the use of the proposed method for realistic metro-network system assessments.

3) ERROR ANALYSIS

As a final step of the experimental validation, we provide an error analysis to quantify the accuracy of the WFLE and FLE models, to assess their conservativeness, and to clearly separate calibration points from blind prediction points.

For each experimental point, the prediction error is defined as

$$\Delta Q^2_{\mathrm{dB}} = Q^2_{\mathrm{dB,meas}} - Q^2_{\mathrm{dB,model}} \tag{67}$$

TABLE 10. Experimental errors versus filtering severity, modulation format, and ROP in the case of Vendor A, considering FLE with 12 taps. Calibration errors are shown in blue. The maximum absolute prediction error is shown in red.

Metric	Modulation	ROP [dBm]	Optical-filter central-frequency shift [GHz]				
			No filter	0	6	7	9
Maximum Absolute Error [dB]	DP-QPSK 200G	-17.5	0.10	0.24	-	0.21	0.05
		-20.0	0.17	0.17	-	0.15	-
		-22.5	0.28	0.15	-	0.21	-
	DP-16QAM 200G	-17.5	0.30	0.23	0.31	-	-
		-20.0	0.27	0.30	0.29	-	-
		-22.5	0.22	0.30	0.33	-	-
	DP-16QAM 400G	-17.5	**0.36**	0.19	-	-	-
		-20.0	0.26	0.22	-	-	-
		-22.5	0.29	**0.13**	-	-	-
RMSE [dB]	DP-QPSK 200G	-17.5	0.06	0.17	-	0.17	0.03
		-20.0	0.07	0.11	-	0.11	-
		-22.5	0.13	0.05	-	0.18	-
	DP-16QAM 200G	-17.5	0.16	0.13	0.16	-	-
		-20.0	0.11	0.12	0.10	-	-
		-22.5	0.08	0.16	0.18	-	-
	DP-16QAM 400G	-17.5	0.15	0.11	-	-	-
		-20.0	0.12	0.09	-	-	-
		-22.5	0.19	**0.07**	-	-	-

TABLE 11. Experimental errors versus filtering severity, modulation format, and ROP in the case of Vendor B, considering FLE with 32 taps. Calibration errors are shown in blue. The maximum absolute prediction error is shown in red.

Metric	Modulation	ROP [dBm]	Optical-filter central-frequency shift [GHz]										
			No filter	0	2	3	4	5	6	7	8	9	10
Maximum Absolute Error [dB]	DP-QPSK 200G	-20.0	0.17	0.24	0.09	0.17	-	0.22	0.18	0.12	0.23	0.09	0.10
		-22.5	0.18	0.38	0.07	0.23	-	0.03	0.06	0.11	0.11	0.25	0.17
	DP-16QAM 200G	-20.0	0.09	0.22	-	-	0.33	**0.42**	0.15	-	-	-	-
		-22.5	0.13	0.23	-	-	0.35	0.20	0.04	-	-	-	-
	DP-16QAM 400G	-20.0	0.10	0.33	0.26	0.32	**0.42**	0.26	0.26	-	-	-	-
		-22.5	0.14	0.21	0.20	0.27	0.15	**0.03**	-	-	-	-	-
RMSE [dB]	DP-QPSK 200G	-20.0	0.09	0.20	0.06	0.09	-	0.19	0.14	0.08	0.18	0.03	0.04
		-22.5	0.12	0.31	0.03	0.19	-	0.02	0.02	0.08	0.08	0.23	0.13
	DP-16QAM 200G	-20.0	0.04	0.14	-	-	0.25	0.29	0.09	-	-	-	-
		-22.5	0.08	0.17	-	-	0.29	0.17	0.04	-	-	-	-
	DP-16QAM 400G	-20.0	0.03	0.28	0.24	0.28	0.39	0.24	0.25	-	-	-	-
		-22.5	0.07	0.17	0.18	0.24	0.13	**0.01**	-	-	-	-	-

With this definition, a positive error means that the model underestimates the measured Q^2_{dB}, and is therefore conservative. Conversely, a negative error indicates that the model overestimates the measured performance.

The resulting error distributions are shown in Figure 22 and Figure 23 for Vendor A and Vendor B, respectively. Calibration points are excluded from the histograms, so that the distributions represent the predictive capability of the calibrated models on blind test data. For Vendor A, saturated DP-QPSK measurements, shown as empty markers in 16a and 16d, are also excluded because the BER reported by the transceiver saturates at very low values and does not provide a reliable Q^2_{dB} estimate. This exclusion rule avoids artificially increasing the apparent model error in a region where the limitation is due to the BER-reporting mechanism rather than to the analytical model.

The histograms in Figure 22 show that, for Vendor A, the errors are concentrated around zero and remain within a narrow range. The WFLE and FLE distributions are very similar, consistent with the fact that, for this transceiver, receiver-side electrical filtering and transceiver-noise coloring are not explicitly modeled because AWGN transceiver noise is assumed; consequently, the two finite-length formulations lead to nearly equivalent predictions. This is confirmed by the detailed error values reported in Table 8 and Table 10, where both the maximum absolute error and the RMSE remain limited over the experimentally accessible combinations of modulation format, ROP, and optical-filter frequency shift. The largest deviations occur in the most stressed filtering

TABLE 12. Summary and comparison of the analyzed equalization models. $N_f\ell$ = number of taps of the equalizer; M = number of optical filters in the considered optical link. The compact complexity notation for FLE refers to the overall dense implementation. The M-dependent contribution is due to colored-noise covariance assembly, while the dense linear-system solution scales as $O((N_f\ell)^3)$.

Model	Disaggregation	Whitening	Complexity	Max Abs. Err. Simulations	Max Abs. Err. Experiments	RMSE Simulations 64 taps	RMSE Experiments
ZFE	✓	✓	$O(1)$	Not available	Not available	Not available	Not available
MMSEE	×	✓	$O(1)$	1.56 dB	Not available	0.12 dB	Not available
FSE	×	✓	$O(1)$	1.56 dB	Not available	0.12 dB	Not available
WFLE	×	✓	$O((N_f\ell)^3)$	0.41 dB	0.54 dB	0.09 dB	0.21 dB
FLE	×	×	$O(M(N_f\ell)^3)$	0.29 dB	0.42 dB	0.09 dB	0.17 dB

configurations, where residual implementation effects and the AWGN-equivalent BER mapping are expected to have a stronger impact.

For Vendor B, the error distributions in Figure 23 show a clearer difference between WFLE and FLE. The FLE distribution is more centered and narrower, whereas the WFLE errors are more spread and generally more conservative. This behavior is expected because the FLE directly includes the sampled colored-noise covariance and the AA-filter response, while the WFLE relies on the whitening approximation. The case used to calibrate the colored TRX-noise PSD and the effective number of taps is not included in the blind-error statistics. Therefore, the errors reported in Table 9 and Table 11 quantify the model prediction capability on withheld ROPs, modulation formats, and optical-filter shifts. The results confirm that the FLE provides the most accurate description for Vendor B, especially when asymmetric filtering and receiver bandwidth limitations make the interaction between colored TRX noise and equalization more relevant.

Tables 8–11 provide a case-by-case view of the maximum absolute error and RMSE as a function of modulation format, ROP, and optical-filter central-frequency shift. Calibration entries are highlighted in blue, separately from blind-prediction entries, while the largest blind-prediction errors are marked in red to identify the most critical configurations. This representation is useful because it avoids relying only on aggregate error metrics and shows how the prediction accuracy evolves with filtering severity. Overall, the errors remain small over the reliable measurement set, supporting the use of the proposed framework for filtering-aware QoT estimation. At the same time, the analysis highlights the expected limitations: strongly filtered conditions, low-ROP operation, and high-symbol-rate DP-16QAM are the most sensitive cases, because small uncertainties in BER, OSNR/ASE loading, ROP, filter characterization, transceiver characterization, or effective equalizer behavior can be amplified into larger Q^2_{dB} deviations.

IV. CONCLUSION

This paper introduced generalized analytical models for filtering penalties and receiver equalization in coherent optical links affected by linear impairments. Starting from a common optical-channel representation and neglecting phase and polarization effects, the analysis jointly considered cascaded wavelength-selective switches, distributed amplified spontaneous emission (ASE) noise, receiver-side transceiver impairments, anti-aliasing filtering, and digital signal processing (DSP) equalization. The resulting formulation provides generic coherent-link metrics, including post-equalization signal-to-noise ratio (SNR), suitable for optical network digital twin (ONDT) transmission modeling.

Closed-form expressions were derived for the zero-forcing equalizer (ZFE), minimum mean-square error equalizer (MMSEE), and fractionally spaced equalizer (FSE), while the whitened finite-length equalizer (WFLE) and finite-length equalizer (FLE) were formulated through semi-analytical matrix models. This unified treatment clarifies the assumptions, accuracy, and complexity of the different equalization approaches. In particular, the ZFE provides a simple disaggregated metric for fast ONDT integration, whereas finite-length equalizers better represent practical receiver DSP.

A key contribution is the generalization of the equalization models to arbitrary normalized transceiver-noise power spectral densities (PSDs). This enables filtering-penalty assessment for commercial transceivers whose noise behavior cannot be accurately described by white-noise assumptions or fixed spectral shapes. The approach is compatible with measurement-based transceiver characterization and does not require access to proprietary implementation details.

The proposed models were assessed through time-domain simulations, highlighting their strengths and limitations in terms of accuracy and complexity. Experiments with two commercial transceivers and accurately characterized optical filters confirm the accuracy of the proposed framework within the operating regions where the devices provide reliable BER estimates. The results show that filtering penalties depend jointly on filter shape, noise distribution, transceiver impairments, received optical power, modulation format, and equalizer implementation.

The final comparison is summarized in Table 12, which reports the overall RMSE together with the main accuracy indicators. The RMSE is computed over all reliable experimental points and, for simulations, over the 64-tap reference data. The FLE provides the most accurate predictions, with maximum absolute errors of 0.29 dB in simulations and 0.42 dB in experiments, and RMSE values of 0.09 dB in simulations and 0.17 dB in experiments. These results support the use of the proposed methods for filtering-aware

QoT estimation in disaggregated metro-access and converged optical networks.

REFERENCES

[1] J.-I. Kani, T. Suzuki, Y. Kimura, S. Kaneko, S.-Y. Kim, and T. Yoshida, "Disaggregation and virtualization for future access and metro networks [invited tutorial]," *J. Opt. Commun. Netw.*, vol. 17, no. 1, pp. A1–A12, 2025, doi: 10.1364/jocn.534303.

[2] E. Agrell et al., "Roadmap on optical communications," *J. Opt.*, vol. 26, no. 9, Sep. 2024, Art. no. 093001, doi: 10.1088/2040-8986/ad261f.

[3] C. Delezoide, P. Ramantanis, and P. Layec, "Weighted filter penalty prediction for QoT estimation," in *Proc. Opt. Fiber Commun. Conf. Expo. (OFC)*, Mar. 2018, pp. 1–3.

[4] D. Wang et al., "Digital twin of optical networks: A review of recent advances and future trends," *J. Lightw. Technol.*, vol. 42, no. 12, pp. 4233–4259, Jun. 1, 2024, doi: 10.1109/JLT.2024.3401419.

[5] H. Nishizawa et al., "Optical network digital twin—Commercialization barriers, value proposition, early use cases, and challenges," 2025, *arXiv:2511.06368*.

[6] V. Curri, "GNPy model of the physical layer for open and disaggregated optical networking [invited]," *J. Opt. Commun. Netw.*, vol. 14, no. 6, pp. C92–C104, Jun. 2022, doi: 10.1364/JOCN.452868.

[7] E. Miotto et al., "Introducing combined effects of filtering and ASE noise in optical links supposing different equalization algorithms," 2025, *arXiv:2504.17408*.

[8] T. Mano et al., "Modeling the input power dependency of transceiver BER-ONSR for QoT estimation," in *Proc. Opt. Fiber Commun. Conf. (OFC)*, 2024, pp. 1–3.

[9] A. Rosso, "Modeling and controlling optical transponder white-boxes based on the physical layer digital twin," *M.S. thesis, Dept. Electron. Telecommun. (DET), Politecnico di Torino*, Turin, Italy, 2024. [Online]. Available: https://webthesis.biblio.polito.it/31825/

[10] A. Rosso et al., "Encompassing filtering effects in transceiver models for converged metro-access networks," in *Proc. Int. Conf. Opt. Netw. Design Model. (ONDM)*, May 2025, pp. 1–6.

[11] D. Pilori, M. Cantono, A. Carena, and V. Curri, "FFSS: The fast fiber simulator software," in *Proc. 19th Int. Conf. Transparent Opt. Netw. (ICTON)*, Girona, Spain, Jul. 2017, pp. 1–4, doi: 10.1109/ICTON.2017.8025002.

[12] A. Pilipetskii et al., "The subsea fiber as a Shannon channel," in *Proc. SubOptic*, 2019, pp. 1–7.

[13] M. Filer, M. Cantono, A. Ferrari, G. Grammel, G. Galimberti, and V. Curri, "Multi-vendor experimental validation of an open source QoT estimator for optical networks," *J. Lightw. Technol.*, vol. 36, no. 15, pp. 3073–3082, Aug. 15, 2018, doi: 10.1109/JLT.2018.2818406.

[14] S. J. Savory, "Digital filters for coherent optical receivers," *Opt. Exp.*, vol. 16, no. 2, pp. 804–817, 2008. [Online]. Available: https://opg.optica.org/oe/abstract.cfm?URI=oe-16-2-804

[15] J. Zhao, Y. Liu, and T. Xu, "Advanced DSP for coherent optical fiber communication," *Appl. Sci.*, vol. 9, no. 19, p. 4192, Oct. 2019. [Online]. Available: https://www.mdpi.com/2076-3417/9/19/4192

[16] A. Carena, V. Curri, G. Bosco, P. Poggiolini, and F. Forghieri, "Modeling of the impact of nonlinear propagation effects in uncompensated optical coherent transmission links," *J. Lightw. Technol.*, vol. 30, no. 10, pp. 1524–1539, May 1, 2012, doi: 10.1109/JLT.2012.2189198.

[17] R. Dar, M. Feder, A. Mecozzi, and M. Shtaif, "Accumulation of nonlinear interference noise in fiber-optic systems," *Opt. Exp.*, vol. 22, no. 12, pp. 14199–14211, 2014. [Online]. Available: https://opg.optica.org/oe/abstract.cfm?URI=oe-22-12-14199

[18] G. Parisi et al., "Analytical QoT estimator of dual-polarization coherent systems with non-integer fractionally-spaced MIMO equalizers," *Opt. Exp.*, vol. 34, no. 12, pp. 21480–21498, 2026. [Online]. Available: https://opg.optica.org/oe/abstract.cfm?URI=oe-34-12-21480

[19] W. Freude et al., "Quality metrics for optical signals: Eye diagram, Q-factor, OSNR, EVM and BER," in *Proc. 14th Int. Conf. Transparent Opt. Netw. (ICTON)*, Jul. 2012, pp. 1–4, doi: 10.1109/ICTON.2012.6254380.

[20] P. Torres-Ferrera et al., "Impact of filtering in optical coherent systems with finite-length equalizers: Modeling and experimental verification," *Opt. Exp.*, vol. 33, no. 20, pp. 41986–42004, 2025. [Online]. Available: https://opg.optica.org/oe/abstract.cfm?URI=oe-33-20-41986

[21] K. Cho and D. Yoon, "On the general BER expression of one- and two-dimensional amplitude modulations," *IEEE Trans. Commun.*, vol. 50, no. 7, pp. 1074–1080, Jul. 2002, doi: 10.1109/TCOMM.2002.800818.

[22] A. Rosso, E. Miotto, E. Virgillito, S. Straullu, and V. Curri, "Is the Gaussian channel model suitable for converged metro-access optical networks?" in *Proc. 25th Anniversary Int. Conf. Transparent Opt. Netw. (ICTON)*, Jul. 2025, pp. 1–4, doi: 10.1109/ICTON67126.2025.11125300.

[23] I. F. de Jauregui Ruiz, A. Ghazisaeidi, T. Zami, S. Louis, and B. Lavigne, "An accurate model for system performance analysis of optical fibre networks with in-line filtering," in *Proc. 45th Eur. Conf. Opt. Commun. (ECOC)*, Sep. 2019, pp. 1–4, doi: 10.1049/cp.2019.1112.

[24] P. Torres-Ferrera, G. Rizzelli, A. Napoli, and R. Gaudino, "Filtering power penalty evaluation of coherent systems affected by ASE and transceiver noise," in *Proc. Int. Conf. Opt. Netw. Design Model. (ONDM)*, May 2024, pp. 1–3, doi: 10.23919/ONDM61578.2024.10582605.

[25] G. Rizzelli, P. Torres-Ferrera, A. Napoli, and R. Gaudino, "Filtering effects characterization in metro-access networks and future high-speed coherent optical communication schemes," *J. Lightw. Technol.*, vol. 43, no. 3, pp. 1114–1122, Feb. 1, 2025, doi: 10.1109/JLT.2024.3477552.

[26] E. Virgillito, S. Straullu, A. Castoldi, F. M. Rodriguez, R. Pastorelli, and V. Curri, "Observation and modeling of filtering penalties in optical switched networks," in *Proc. 24th Int. Conf. Transparent Opt. Netw. (ICTON)*, Jul. 2024, pp. 1–4, doi: 10.1109/ICTON62926.2024.10647862.

[27] R. Gholamipourfard, A. Ghazisaeidi, and R. S. B. Ospina, "A complexity-aware theoretical framework for the performance analysis of linear MIMO equalizers in coherent spatial-division multiplexing transmission systems," *J. Lightw. Technol.*, vol. 43, no. 11, pp. 5189–5201, Jun. 15, 2025, doi: 10.1109/JLT.2025.3546455.

[28] G. Parisi, P. Torres-Ferrera, G. Rizzelli, R. Gaudino, and A. Napoli, "Analytical model for filtering impact estimation of coherent systems with finite-length equalizer," in *Proc. Int. Conf. Opt. Netw. Design Model. (ONDM)*, May 2025, pp. 1–3, doi: 10.23919/ONDM65745.2025.11029352.

[29] J. G. Proakis, *Digital Communications*, 5th ed., New York, NY, USA: McGraw-Hill, 2007.

[30] J. Cioffi. 'Equalization', *Stanford Chapters on Digital Transmission*. Accessed: Apr. 3, 2026. [Online]. Available: https://cioffi-group.stanford.edu/

[31] J. Cioffi. 'Spectral Factorization and Scalar Filter Realization', *Stanford Chapters on Digital Transmission*. Accessed: Apr. 3, 2026. [Online]. Available: https://cioffi-group.stanford.edu/

[32] T. Rahman et al., "On the mitigation of optical filtering penalties originating from ROADM cascade," *IEEE Photon. Technol. Lett.*, vol. 26, no. 2, pp. 154–157, Jan. 1, 2014, doi: 10.1109/LPT.2013.2290745.

[33] G. Rizzelli, M. Casasco, A. Pagano, V. Ferrero, and R. Gaudino, "Experimental demonstration of in-field 400G coherent metro-access convergence," in *Proc. Opt. Fiber Commun. Conf. (OFC)*, 2024, pp. 1–14. [Online]. Available: https://opg.optica.org/abstract.cfm?URI=OFC-2024-W1J.1

[34] Y. Sakamaki, T. Kawai, T. Komukai, M. Fukutoku, and T. Kataoka, "Evaluation of optical filtering penalty in digital coherent detection system," *IEICE Commun. Exp.*, vol. 1, no. 2, pp. 54–59, 2012, doi: 10.1587/comex.1.54.

[35] E. Miotto et al., "QoT impairments induced by statistical filtering variations with a realistic equalizer," in *Proc. Eur. Conf. Opt. Commun. (ECOC)*, Sep. 2025, pp. 1–4.

[36] J. Pan and S. Tibuleac, "Real-time ROADM filtering penalty characterization and generalized precompensation for flexible grid networks," *IEEE Photon. J.*, vol. 9, no. 3, pp. 1–10, Jun. 2017, doi: 10.1109/JPHOT.2017.2699642.

[37] L. Galdino et al., "On the limits of digital back-propagation in the presence of transceiver noise," *Opt. Exp.*, vol. 25, no. 4, pp. 4564–4578, 2017. [Online]. Available: https://opg.optica.org/oe/abstract.cfm?URI=oe-25-4-4564

[38] C. Xie et al., "Open and disaggregated optical transport networks for data center interconnects [invited]," *J. Opt. Commun. Netw.*, vol. 12, no. 6, pp. C12–C22, Jun. 2020. [Online]. Available: https://opg.optica.org/jocn/abstract.cfm?URI=jocn-12-6-C12

[39] C. Delezoide, P. Ramantanis, and P. Layec, "On the performance prediction of optical transmission systems in presence of filtering," in *Proc. 19th Int. Conf. Transparent Opt. Netw. (ICTON)*, Jul. 2017, pp. 1–4, doi: 10.1109/ICTON.2017.8024998.

[40] Q. Zhuge et al., "Building a digital twin for intelligent optical networks [invited tutorial]," *J. Opt. Commun. Netw.*, vol. 15, no. 8, pp. C242–C262, 2023. [Online]. Available: https://opg.optica.org/jocn/abstract.cfm?URI=jocn-15-8-C242

[41] P. Agrawal, *Loss Management*. Hoboken, NJ, USA: Wiley, 2010, ch. 7, pp. 295–344. [Online]. Available: https://onlinelibrary.wiley.com/doi/abs/10.1002/9780470918524.ch7

[42] H. H. Zeng and L. Tong, "Blind equalization using the constant modulus algorithm," in *Proc. 3rd Int. Conf. Signal Process. (ICSP96)*, vol. 1, May 1996, pp. 400–403, doi: 10.1109/ICSIGP.1996.567287.
[43] C. Pulikkaseril, L. A. Stewart, M. A. F. Roelens, G. W. Baxter, S. Poole, and S. Frisken, "Spectral modeling of channel band shapes in wavelength selective switches," *Opt. Exp.*, vol. 19, no. 9, pp. 8458–8470, 2011. [Online]. Available: https://opg.optica.org/oe/abstract.cfm?URI=oe-19-9-8458
[44] D.-J. Jwo, W.-Y. Chang, and I.-H. Wu, "Windowing techniques, the Welch method for improvement of power spectrum estimation," *Comput., Mater. Continua*, vol. 67, no. 3, pp. 3983–4003, 2021, doi: 10.32604/cmc.2021.014752.
[45] E. Temprana, B. Huebner, J. Geyer, and T. Williams, A Receiver-Agnostic Approach to ETCC, *Standard IEEE* 802.3, Nov. 2025. [Online]. Available: https://www.ieee802.org/3/dj/public/2511/temprana3dj01a2511.pdf



ENRICO MIOTTO (Graduate Student Member, IEEE) received the B.Sc. degree (summa cum laude) in information engineering from the Universitá degli Studi di Padova in 2022 and the M.Sc. degree (summa cum laude) in communications engineering, specializing in optical fiber communications from the Politecnico di Torino, Italy, in 2024, where he is currently pursuing the Ph.D. degree with the Open PLANET Laboratory Research Group, Department of Electronics and Telecommunications. His research interests encompass optical networking, with a focus on mathematical and physical electromagnetic modeling applied to optical communications. His recent publications address system margin assessment of filtering penalty and polarization-dependent loss due to wavelength-selective switches, specifically regarding quality of transmission estimation for the development of an optical network digital twin. He is a Student Member of Optica and an active member of the Optica student chapter in Turin.



ANDREA ROSSO (Graduate Student Member, IEEE) received the M.Sc. degree (summa cum laude) from the Politecnico di Torino, Italy, with a thesis on transceiver modeling and characterization for optical communication systems, where he is currently pursuing the Ph.D. degree in telecommunications engineering. He is also a member of the PLANET Research Group, where his work focuses on enhancing optical networks through the integration of open network control architectures with physical-layer awareness. His research interests include optical channel modeling, device characterization, and the study of underlying physical phenomena affecting optical transmission.



STEFANO STRAULLU (Senior Member, IEEE) received the Graduate degree in telecommunications engineering from the Politecnico di Torino, Turin, Italy, in 2005, and the Ph.D. degree in electronics and communications engineering from the Politecnico di Torino, with a thesis on next-generation passive optical networks. His Graduate thesis on the realization and testing of opto-electronic subsystems for packet-switched optical networks, completed in the PhotonLab, Istituto Superiore Mario Boella, Turin. Since May 2009, he has been a Researcher at the Istituto Superiore Mario Boella (now LINKS Foundation) of Turin, Optical Communication Unit. He has published more than 120 journals and conference papers. His main research interests are focused on the performance analysis and design of optical transmission systems and the application of digital signal processing techniques in optical links.



EMANUELE VIRGILLITO (Senior Member, IEEE) was born in Catania, Italy, in June 1989. He received the B.Sc. degree in telecommunication engineering from the University of Catania in 2013, the M.Sc. degree in telecommunication engineering from the Politecnico di Torino in 2016, with a thesis on multicore optical fiber systems abroad at the Instituto Superior Tecnico, Lisbon, and the Ph.D. degree from the Politecnico di Torino in 2021, with a thesis on the observation and modeling of physical-layer phenomena in open optical networks. He is currently an Assistant Professor with the Politecnico di Torino. His research activity is mainly focused on the study of the physical-layer impairment for the orchestration and management of modern open and disaggregated optical networks. He is also involved in environmental sensing using telecommunications optical fiber systems.



RAFFAELE CORSINI received the M.Sc. degree in physics from the Universitá degli Studi di Milano in 1993. He has more than 30 years of experience in the field of fiber-optic telecommunication systems, gained in the most important Italian companies in the sector (Pirelli, Pirelli Laboratories, SM-Optics). He was also a Researcher with the Scuola Superiore Sant'Anna in Pisa for five years. He is currently the Director of the WDM Group, SM-Optics.



ANDREA BOVIO received the B.Sc. and M.Sc. degrees in telecommunications engineering from the Politecnico di Milano in 2017 and 2019, respectively. He is currently a Research and Development Engineer with the Photonics Department, SM-Optics S.r.l., Cologno Monzese, Italy. His work focuses on the development of the company's Optical Design and Planning Tool, contributing to the definition of algorithms and modeling techniques for signal propagation in optical fibers and the optimization of network dimensioning.

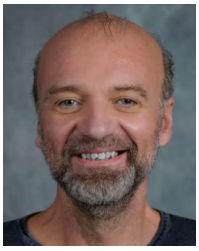

VITTORIO CURRI (Fellow, IEEE) received the Laurea degree (cum laude) in electrical engineering and the Scientific Ph.D. degree in optical communications from the Politecnico di Torino (PoliTO), Italy, in 1995 and 1999, respectively. He is currently a Founder Member of the OptCom Group and PhotonLab, PoliTO, and also leads the Open PLANET Laboratory. He is also a Full Professor with the Department of Electronics and Telecommunications, PoliTO. He has been a Visiting Scholar at Stanford University and the University of California, Santa Barbara. He is the co-author of more than 550 scientific publications. His major research interests are in fiber transmission modeling, including nonlinearities, transmitter and receiver optimization, design strategies for optical links, Raman amplification and simulation, and modeling of optical communication systems. He is one of the early promoters of using multi-band transmission in single-mode fibers. He is also active in the analysis of the impact of physical layer on networking for planning and control of open and disaggregated optical networks based on vendor-neutral digital twins, including artificial-intelligence techniques. He is also the Scientific Chair of the GNPy open-source project within the industry consortium Telecom Infra Project. He is also an early promoter of using the optical network as a sensor. He is an Optica Fellow and an AAIA Fellow.